Aerospace Science and Technology 168 (2026) 111129

Contents lists available at ScienceDirect

Aerospace Science and Technology

journal homepage: www.elsevier.com/locate/aescte

Robust equalization of multi-lane electromechanical actuators: Comparative analysis of torque-summed and velocity-summed architectures

Fawaz Y Annaz

Department of Engineering, Birmingham City University, Birmingham, West Midlands B4 7BD, United Kingdom

ARTICLE INFO

Edited by: Dr Jérôme Morio

Keywords:
All-electric aircraft
Electromechanical actuators
Safety-critical systems
Torque and Velocity summed architectures
Equalisation strategies (force and lane equalisation)
Sensor drift
Adaptive and robust control

ABSTRACT

The increasing demand for energy-efficient, low-emission aircraft has accelerated the transition toward all-electric aircraft (AEA), driving the need for highly reliable electromechanical actuators (EMAs) in flight-critical systems. A major challenge in multi-lane EMA configurations lies in torque and velocity disparities caused by component mismatches, sensor drift, and mechanical tolerances. These discrepancies can result in force-fight, increased mechanical stress, and reduced control accuracy, necessitating robust equalisation strategies. This study investigates force equalisation and lane equalisation in torque-summed and velocity-summed EMA architectures to mitigate lane-torque disparities (ΔT) and enhance system robustness. A four-lane redundant EMA system, originally designed to actuate the inboard aileron of the Sea Harrier aircraft, was modelled in MATLAB–Simulink with a proportional–integral–derivative (PID) controller and Monitoring–Voting–Averaging Devices (MVADs) for feedback processing. Three-phase motor models were included to capture torque-ripple effects, and simulations were conducted across a range of inertial and aerodynamic load conditions. The results show that force equalisation effectively reduces lane-torque disparities in torque-summed architectures, improving load sharing and resilience under tachometer and potentiometer drift. In contrast, the velocity-summed architecture is inherently torque-balanced (lane-torque disparity ΔT is approximately zero), so lane equalisation has limited effect on ΔT. A potentiometer bias appears as a steady tracking offset that equalisation alone does not remove. These findings highlight critical trade-offs between architectures and underscore the importance of advanced equalisation and adaptive control strategies to further optimise EMA performance in next-generation all-electric aircraft. Although framed by an aerospace EMA, the methods and conclusions are not domain specific. The closed-form equalisation laws, cross-monitoring, and analysis of sensor-bias mechanisms generalise to multi-lane system architectures in robotics, automotive drive-by-wire, industrial automation, wind-turbine blade-pitch control, marine actuation, and medical and assistive devices.

1. Introduction

In recent years, energy-efficient, low-emission aircraft designs have become a major focus for aircraft designers, airline companies, and manufacturers [1–3]. This shift has driven increased demand for all-electric aircraft (AEA) within the aerospace engineering sector. This paper contributes to these efforts and builds on previous work by comparing the torque and velocity summed assemblies shown in Figs. 1a and 1b Both designs meet the redundancy requirements (fail--operational/fail-safe) mandated for flight-critical applications [4]. The paper presents recent findings from a program that was initiated in the 1990′s at Queen Mary University of London, which has advanced the AEA concept and consolidated all secondary power systems into a single electric power system.

The designs consist of architectures with four actuators driving a common shaft-gearbox assembly. In both architectures, it was assumed that the actuator would experience one failure at a time, which could be caused by a motor or feedback transducer (FT) malfunction. It was shown that motor failures had the most significant impact on the actuation system’s response, and consequently, the aircraft’s roll response [5]. Generally, when a failure is detected, an alarm is triggered, and the failure is isolated. In the case of a motor failure, in addition to electrical isolation, the motor must be mechanically disengaged either by activating clutches in the torque summed architecture (T_ΣA) or brakes in the velocity summed architecture ($V_\Sigma A$).

E-mail address: fawaz.annaz@bcu.ac.uk.

https://doi.org/10.1016/j.ast.2025.111129
Received 6 June 2025; Received in revised form 16 October 2025; Accepted 20 October 2025

List of symbols and abbreviations

Abbreviations

AEA – All-Electric Aircraft
EHA – Electro-Hydrostatic Actuator
EMA – Electromechanical Actuator
FT – Feedback Transducer
MEA – More-Electric Aircraft
PID – Proportional-Integral-Derivative
MVAD – Monitoring-Voting-Averaging Device
SHA – Servo-hydraulic actuator

Architecture

T_Σ – Torque-summing
$T_\Sigma A$ – Torque-summed architecture
V_Σ – Velocity-summing
$V_\Sigma A$ – Velocity-summed architecture

Equalisation

F_{eq} – Force Equalisation
L_{eq} – Lane Equalisation
$\overline{x}$ – Averaged feedback signal (position or velocity)
x_i – Feedback signal of lane i
N_h – Number of healthy (unisolated) sensors

System variables

$\alpha_G{}^o$ – Angle of incidence with respect to M
$\delta_a{}^o$ – Aileron Deflection
$\delta_a|_{\pm 18^o, M=0.2}$ – Aileron deflection at $\pm 18^o$during low aircraft speed ($M = 0.2$)
$\delta_{x}|_{M=0.8}$ – Aileron Angle at $M = 0.8$ that gives Zero Aerodynamic load
ω – Angular velocity (tachometer reading)
θ – Shaft angle
T_i – Torque contribution of lane i
T_A- –Total aerodynamic torques
$T_{A_v}-$ –Torques due to aerodynamic variable component
$T_{A_s}-$ –Torques due to aerodynamic steady component
T_I- –Torques due to Inertial load
T_{out} – Total output driving torque
ΔT – Torque disparity
ΔT_{np} – Torque disparity between lanes n and p
G – Gearbox ratio
I_n – Phase current
$K_{T,i}$ – Motor torque constant of lane i
L_i – Inductance of lane i
M – Mach number $0.2 \leq M \leq 1.0$
$K_{e,i}$ – Back EMF constant of lane i
R_i – Winding resistance of lane i

Motor/feedback models

I_n – Phase current
M_{nom} – Motor with nominal parameters
FT_{nom} – Feedback transducer with nominal readings
$M_{Tmax\pm}$ – Maximum torque motor mismatch case
Pot_i – Potentiometer reading of lane i
$Tacho_i$ – Tachometer reading of lane i

The main aim of this paper is to evaluate the impact of force equalisation (F_{eq}) and lanes equalisation (L_{eq}) in reducing or eliminating disparities between inherently mismatched lanes in the T_Σ and V_Σ architectures, while the actuators is experiencing drift in FT readings.

While this study is motivated by evaluating force and lane equalisation under drift conditions, it also addresses a broader research gap. Despite extensive work on equalisation in hydraulic and hybrid actuation systems, very few studies have systematically investigated torque-summed and velocity-summed electromechanical architectures under realistic non-idealities such as torque ripple, sensor drift, and inter-lane mismatches. This gap is critical, as such disparities can compromise equalisation strategies and degrade reliability in flight-critical applications. The present work therefore provides the first systematic evaluation of both architectures under these adverse conditions, establishing evidence-based design guidelines to enhance the robustness and reliability of all-electric aircraft actuation systems.

Strengths and contributions. This study (i) provides a fully electromechanical, system-level comparison of $T_\Sigma A$ and $V_\Sigma A$ multi-lane EMAs under realistic non-idealities, including torque ripple, inter-lane mismatch, and sensor bias and drift; (ii) formalises closed-form equalisation laws (F_{eq}, L_{eq}) and a quantile-based screening policy for maximum torque mismatch and sensor bias and drift; and (iii) articulates design recommendations for when equalisation materially reduces lane-torque disparity, versus when averaging biased feedback mainly manifests as tracking error.

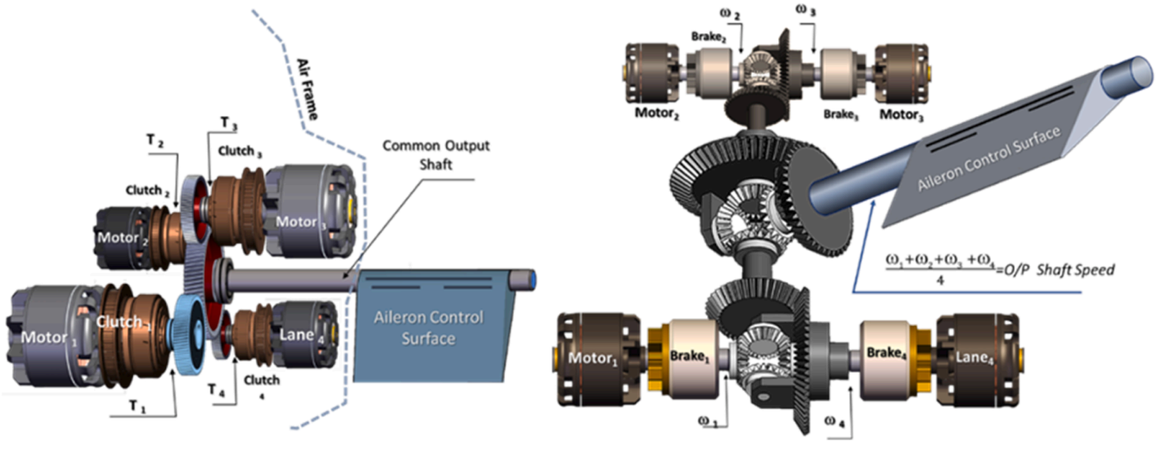

a) Torque-Summing (T_Σ) b) Velocity-Summing (V_Σ)

Fig. 1. The two proposed electromechanical architectures.

Study aim and objectives

Aim. Establish an evidence-based, fully electromechanical comparison of torque-summed (T_ΣA) and velocity-summed (V_ΣA) multi-lane EMAs under realistic non-idealities, including torque ripple, inter-lane mismatch, and sensor bias and drift; and assess the effectiveness of force equalisation (F_{e_q}) and lane equalisation (L_{e_q}) in mitigating lane disparities and preserving control performance.

To operationalise these contributions, the study pursues the following objectives:

1. **Common modelling framework.** Formulate a matched MATLAB/Simulink framework for both architectures, comprising the electromechanical dynamics of a four-lane EMA with BLDC drives (including commutation torque ripple), aerodynamic and inertial loads, a single baseline PID ($K_p = 30,\ K_i = 6s^{-1},\ K_d = 1$) position controller, and MVAD-based cross-monitoring of potentiometers and tachometers.
2. **Equalisation laws and monitoring.** State the closed-form sharing/equalisation laws (F_{e_q}, L_{e_q}) and the MVAD thresholding policy using one-sided predictive quantiles at $p = 0.9999$ (false-alarm probability 10^{-4}) to set screening thresholds for: (i) maximum torque mismatch and (ii) sensor bias/drift across redundant feedback channels.
3. **Scenario set and metrics.** Quantify effects on lane-torque disparity (ΔT), position (velocity) tracking error, and qualitative stability across: (i) nominal parameters, (ii) maximum torque mismatch ($M_{Tmax\pm}$), and (iii) drift in tachometer and potentiometer channels (single-lane and two-lane).
4. **Architecture-specific behaviours:** Identify when T_ΣA benefits materially from F_{e_q} in reducing ΔT, and when V_ΣA is inherently torque-balanced yet susceptible to averaging of biased feedback that introduces steady-state tracking error.
5. **Design guidance.** Consolidate findings into practical guidance on architecture and equalisation choices under drift and mismatch, noting the limits of bias averaging and outlining mitigation options such as bias observers and sensor redundancy with voting or exclusion.

2. Redundancy and electrification of aircraft

2.1. The evolution of aircraft electrification and redundant actuation systems

The progression toward aircraft electrification has undergone two primary phases: the More-Electric Aircraft (MEA) and the AEA. The MEA phase marked the transition from traditional mechanical, hydraulic, and pneumatic subsystems to partially electric alternatives, whereas the AEA phase aimed for a complete consolidation of all secondary power systems into a single electrical power source [6,7]. These advancements significantly impacted onboard actuation systems, leading to the increasing adoption of EMAs as replacements for traditional hydraulic actuators (HAs).

The shift from hydraulic to electromechanical actuation was driven by the potential reductions in power consumption, mass, noise, and maintenance requirements [1]. However, this transition also introduced new challenges, making the MEA an intermediary step before achieving full aircraft electrification [8,9]. Various studies have examined the reliability and survivability of EMA systems in critical flight control applications, including the "Electromechanical Actuator Systems Survivability, Vulnerability, and Fault Tolerance Test" program, which explored EMA implementation in future fighter aircraft [10–12]. Further recent studies have explored the integration of machine learning and deep learning techniques for the health monitoring of EMAs [13,14].

Historically, aircraft flight control systems relied exclusively on hydraulic actuators due to their robustness and the absence of viable alternatives. The development of BLDC motors and advancements in electronic control systems enabled the transition to EMAs, allowing for complete electrification of aircraft actuation systems [15,16]. This shift led to the introduction of redundant architectures to ensure fail-operational and fail-safe actuation, which is crucial for flight-critical applications.

2.2. The role of redundancy in electromechanical actuation

Redundant actuation systems are designed to ensure continued operation despite the failure of individual components. Fig. 2 illustrates early redundancy mechanisms, such as Force Voting, Velocity Summing, and Position Summing Systems [17,18]. These architectures sought to address mismatches between redundant actuators operating in either active or standby modes. To eliminate force fight, load sharing was implemented in multiple-actuator systems with identical inputs, ensuring that the joint contributions achieve the demanded output position.

To further minimize force fight and ensure acceptable load sharing, the following four methods are commonly employed: Accurate Tolerance Control of the actuator feedback loop to reduce discrepancies between channels; Compliance Between Channels to allow for flexibility and accommodate minor differences in actuator outputs; Low Force Gain Actuators, achieved by using low-pressure-gain servo-valves to reduce sensitivity and mitigate load imbalances; and Equalisation to ensure balanced load distribution across channels [17,18] .

A key concern in redundant actuation is force fight, which occurs when multiple actuators operating in active/active mode generate conflicting outputs. This issue is particularly pronounced in multi-lane architectures, where actuator mismatches can lead to torque imbalances, degraded performance, and mechanical wear. Several studies, including those in [19,20], have addressed force fight by proposing force equalisation strategies in multi-actuator architectures. These studies demonstrate the effectiveness of hybrid control methodologies in mitigating torque imbalances and mechanical stress.

2.3. Prior research in equalisation strategies

Numerous studies have investigated force equalisation in redundant actuator systems, yet only a few have specifically addressed lane equalisation in torque-summed and velocity-summed architectures.

While previous studies have advanced equalisation concepts in hybrid electrohydraulic and electromechanical systems, their scope has been limited in key respects. Table 1 provides a structured comparison between representative prior approaches and the present work. This highlights that most prior research either focused on hybrid configurations, rig-level testing, or torque-summed EMAs only, without a systematic comparison against velocity-summed architectures under realistic non-idealities. The present study extends this body of work by conducting the first systematic evaluation of both architectures under torque ripple, sensor drift, and lane mismatches, and by deriving practical design guidelines for fully electromechanical multi-lane systems.

2.3.1. Hybrid actuation and redundant control strategies

Several research efforts have focused on hybrid actuation approaches, integrating hydraulic and electromechanical actuators to enhance reliability. The authors in [23,24] categorized hybrid actuation into two primary operational modes: Active/Passive Mode: A single actuator operates at a time, preventing force fight between redundant lanes; and Active/Active Mode: Multiple actuators function simultaneously, increasing the risk of force fight, potentially affecting control accuracy and causing structural stress [25].

Wang et al. [26] examined force equalisation techniques in hybrid actuation systems, proposing three control strategies (Fig. 3): Position Control with Compensated Feedback: Synchronizing sensor offsets to

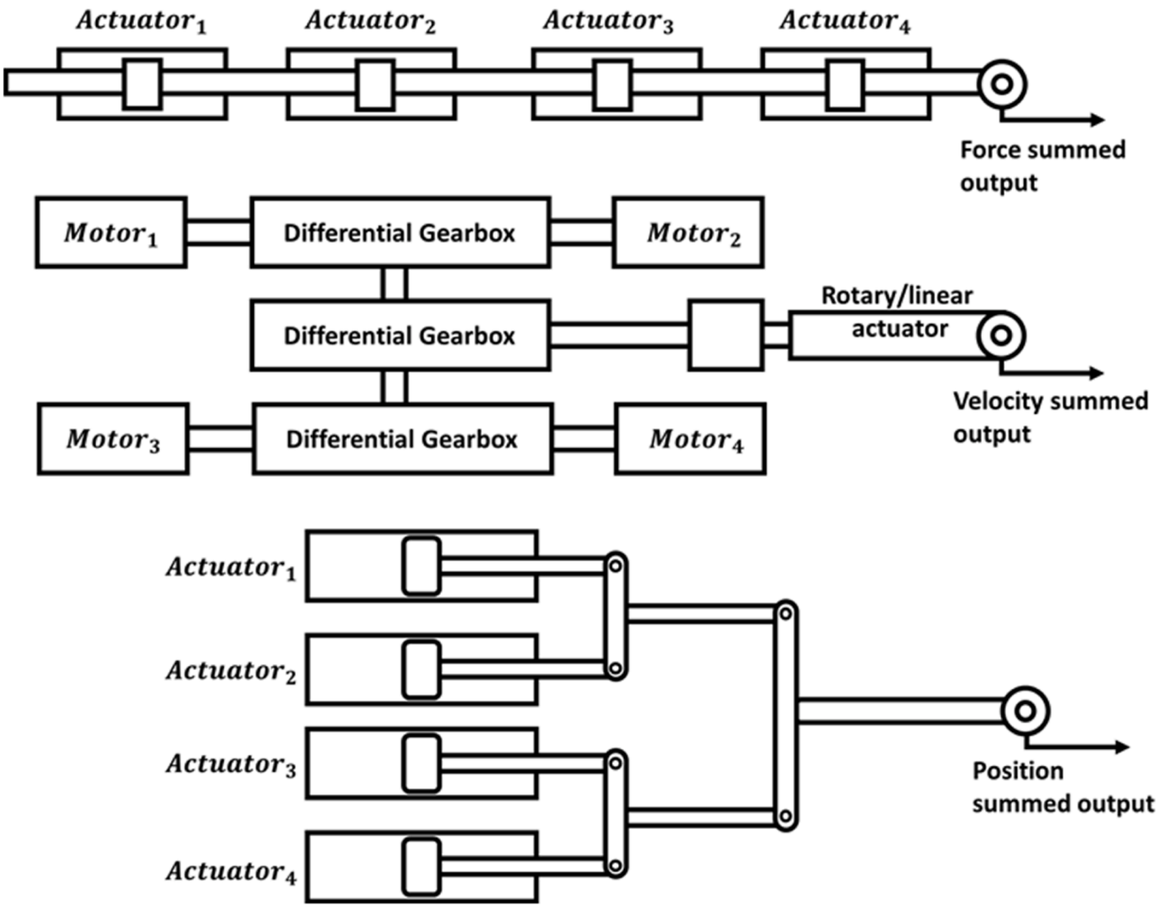

Fig. 2. Early consolidation mechanizations that dealt with mismatched inputs.

Table 1
Comparison of existing equalisation strategies with the proposed approach.

Study	System Type	Focus	Limitations	Present Study Contribution
Wang & Maré (2014) [19]	Hybrid EHA/ EMA	Force equalisation in redundant actuation	Limited to hybrid systems; no treatment of lane mismatches in full EMAs	Extends equalisation analysis to fully electromechanical torque- and velocity-summed architectures
Hoffman (2018) [21]	EMA test rig	Experimental testing of equalisation	Rig-level only; no aircraft-level scenarios; drift effects not studied	Provides systematic simulation of drift, mismatches, and torque ripple across architectures
Annaz (2020, 2024) [22,21]	Torque-summed EMAs	Force equalisation effectiveness	Did not compare with velocity-summed architectures	First direct comparison of torque- vs. velocity-summed EMAs under drift and mismatches
Present Study	Torque- and velocity-summed EMAs	Force and lane equalisation under practical non-idealities	Not applicable as this work is the first systematic comparison; limitations are discussed separately in Section 7	Provides the first systematic comparison and design guidelines for fully electromechanical multi-lane architectures

ensure alignment; Position Control with Force Compensation: Adjusting EMA output force to match SHA force; and Zero-Force Output for Redundant Actuators: Preventing force fight in active/active configurations.

Additional research, including [27,28], has refined these control techniques, emphasizing synchronization to mitigate force disparities. Studies such as [19,20] further developed feedforward-based fractional-order control methods, improving overall actuator coordination.

Wang and Maré [29,19] extended this research by investigating force equalisation in electrohydraulic and electromechanical hybrid actuation systems for aileron control, as illustrated in Fig. 4. Their findings demonstrated that equalisation improved static torque balancing but did not fully address dynamic disparities. Moreover, their study did not account for power source consolidation, as their test configurations included both hydraulic and electric actuation.

While the studies in Table 1 demonstrate the importance of force equalisation and redundancy in hybrid or electro-hydrostatic configurations, their findings remain limited by partial electrification, rig-level testing, or the exclusion of velocity-summed electromechanical architectures. The present work extends this body of research by performing a fully electromechanical system-level comparison of T_Σ and V_Σ EMAs architectures under realistic non-idealities, including torque ripple, inter-lane mismatch, and sensor drift. This systematic analysis establishes the first comprehensive evidence base for equalisation strategies in multi-lane EMAs operating within the All-Electric Aircraft framework.

2.3.2. *Experimental validation and real-world implementations*

To validate equalisation strategies, Hoffman [21] developed a passive electromechanical test rig in collaboration with the Air Force Research Laboratory and MOOG Aerospace. The rig simulated dynamic

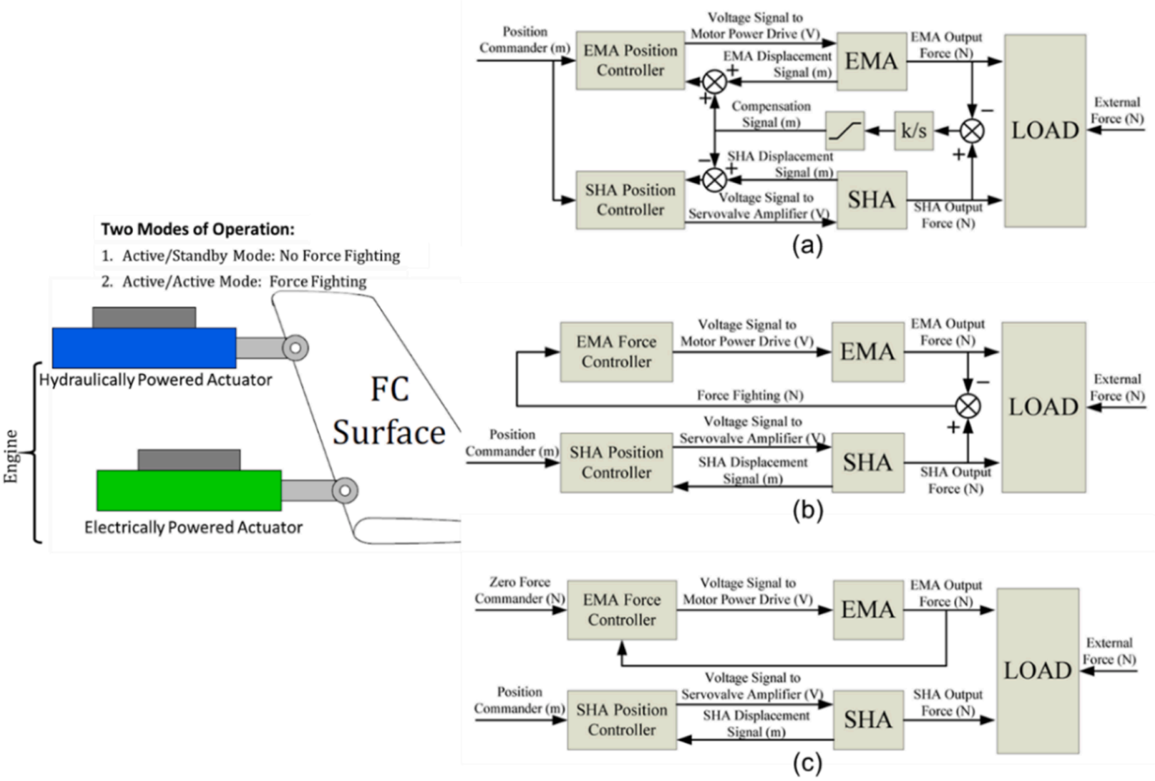

Fig. 3. Servo-hydraulic actuator and electromechanical actuator hybrid systems.
(a) SHA Position Control/EMA Position Control.
(b) SHA Position Control/EMA Force Control.
(c) SHA Position Control/EMA No-Load Control.

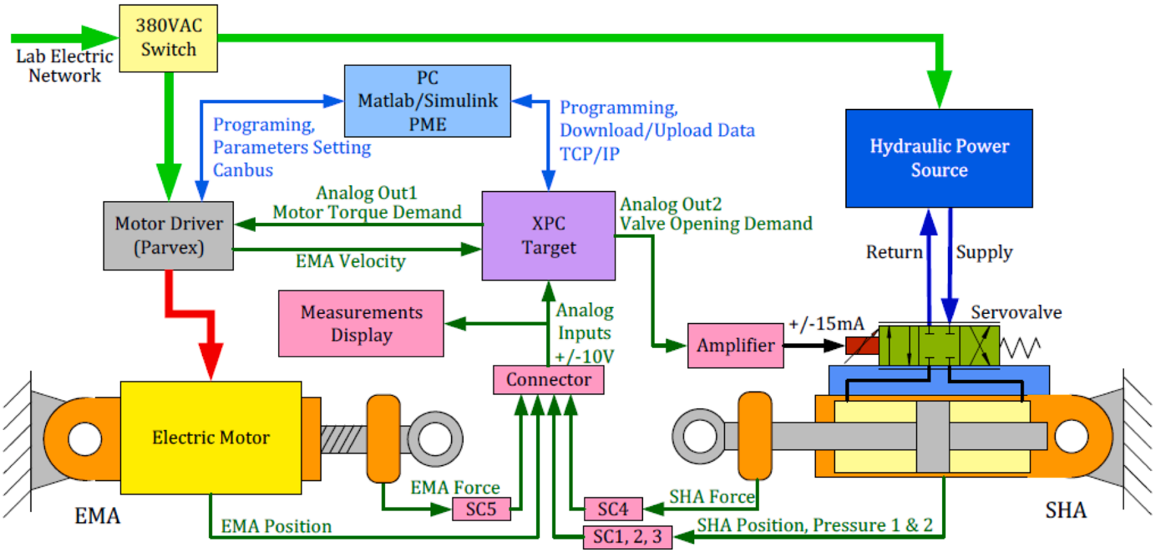

Fig. 4. Control system schematic of test bench [29].

electromechanical actuation conditions but lacked full in-flight validation. Subsequent studies refined the methodology by integrating real-time control algorithms and expanding testing scenarios [30].

Other studies have explored force equalisation in different actuator configurations:

- Boehringer et al. [31] examined force equalisation in hydraulic actuation systems. The author proposed monitoring pressure sensors to closely align the actuators' positions in the system.
- Lin et al. [32] investigated synchronization techniques to mitigate force disparities in X-38 flap actuators.
- Bucci et al. [25] highlighted force fight issues in active/active redundant actuator setups.
- Wang et al. [26,29,19] developed control strategies for achieving static force equalisation in redundant actuation architectures.

Research efforts, including [33,34,35] have examined fault detection methodologies within redundant actuators, focusing on predictive maintenance through machine learning models. These efforts enhance real-world applicability by allowing proactive system monitoring. Studies such as [14,27,28] have examined force fight issues in active/-active redundant actuator setups, highlighting the necessity of equalisation strategies.

2.3.3. *Adaptive control and advanced monitoring techniques*

Recent research has also explored adaptive control methods to enhance equalisation. Rehman et al. [36] introduced Model Reference Adaptive Control for synchronizing hydraulic and electro-hydrostatic actuators (EHAs), as shown in Fig. 5. The Airbus A380's hybrid actuation system exemplifies this approach, as documented in [37].

Annaz [22] investigated force equalisation in torque-summed architectures, demonstrating that while equalisation reduced torque disparities due to high component tolerances or dormant failures, it did not fully compensate for inherent lane mismatches (Fig. 6). Further research is needed to address these residual disparities and improve system stability.

The studies in [33,14] integrated machine learning to driven monitoring, thus providing real-time adjustments to equalisation controllers. The use of adversarial neural networks for fault detection in [33] presents a novel approach to identifying actuator mismatches before failure occurs.

2.3.4. *Fault detection and health monitoring*

The role of fault detection and health monitoring has expanded with the increasing complexity of redundant actuation systems. Some of the studies that have focused on fault detection and health monitoring for redundant actuator systems:

- Di Rito and Schettini [38] developed real-time model-based algorithms to detect faults in UAV EMA flight control systems.
- Di Rito et al. [39] introduced a fault detection system for dual-motor velocity-summed linear actuators, capable of identifying jamming and drift conditions.

More recent research, including [13,14], has emphasized deep learning-based predictive maintenance, ensuring early fault detection

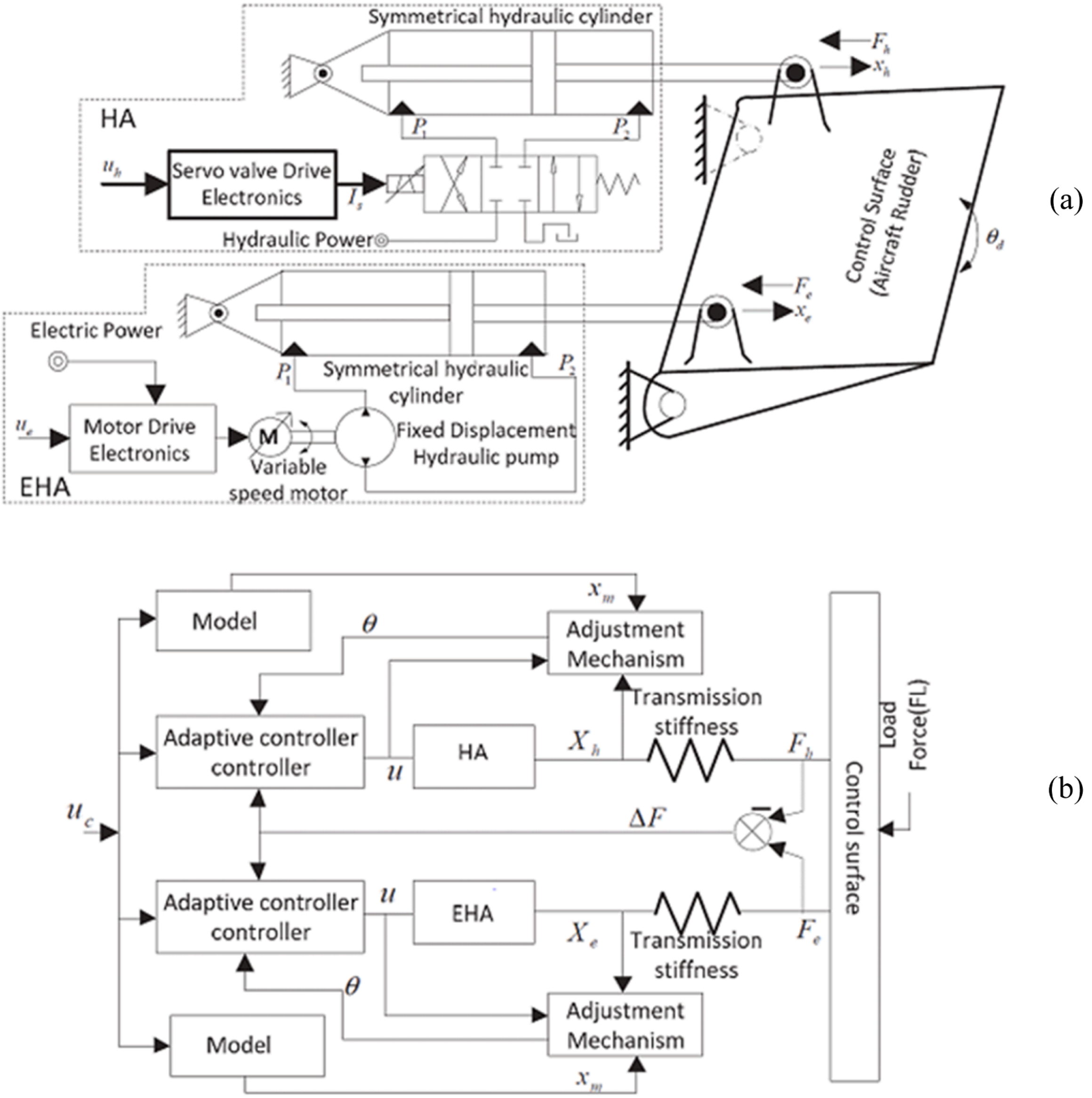

Fig. 5. Redundant actuation system with adaptive control [36].
(a) Structure of redundant actuation system.
(b) Adaptive control of HA/EHA system.

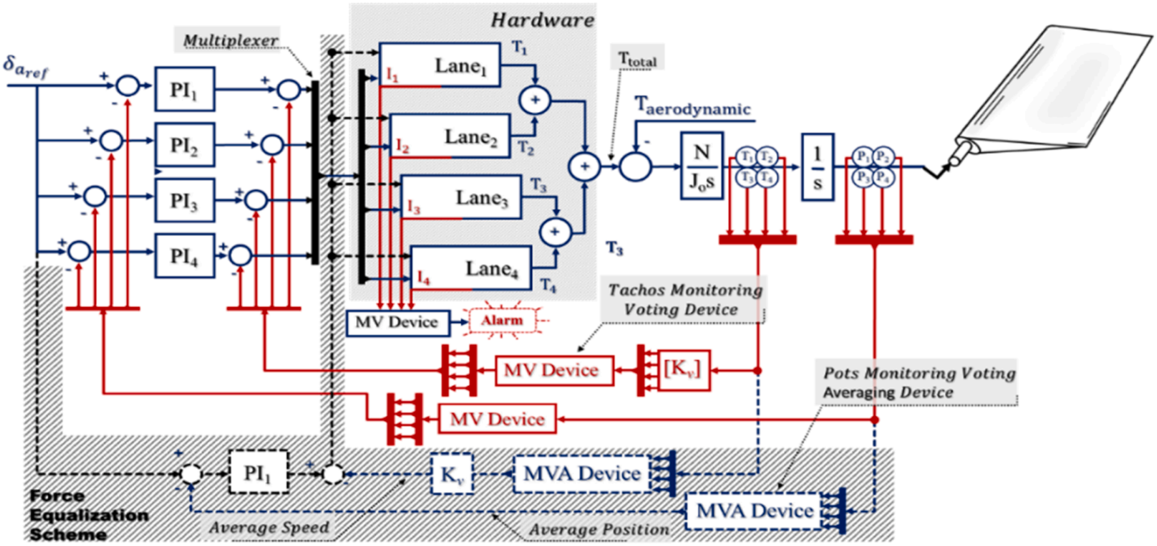

Fig. 6. T_Σ architectures with and without force equalisation (F_{eq}) schemes [22]; shaded blocks indicate the equalisation path.

and prevention [35]. reviewed fault detection methodologies for railway point machines, offering parallels to electromechanical actuator diagnostics in aerospace applications.

2.4. Monitoring channels and threshold definition

Despite extensive research on force equalisation, most prior studies have primarily focused on hydraulic or hybrid electrohydraulic systems. Fewer investigations have specifically addressed lane equalisation in multi-lane EMAs, particularly those employing torque-summed or velocity-summed configurations [40,41].

This study seeks to bridge this gap by evaluating force and lane equalisation techniques in fully electromechanical architectures, emphasising their impact on mitigating torque disparities, sensor drift effects, and redundancy-related inconsistencies. The findings contribute to the development of more robust and efficient multi-lane electromechanical actuator systems for next-generation aircraft.

For this application, motors, potentiometers, and tachometers are monitored for faults; thresholds for each device are one-sided predictive quantiles set to a false-alarm probability of 10^{-4} ($p = 0.9999$; 0.01 %), following [[5], Fig. 9; Secs. 11–13].

This work contributes a side-by-side evaluation of T_Σ and V_Σ multi-lane EMAs under realistic non-idealities (i.e., lane mismatch, sensor drift, and torque ripple). It integrates an MVAD cross-monitoring framework with closed-form force/lane equalisation laws. It also provides evidence-based design guidance on when F_{eq}/L_{eq} reduce lane-torque disparity ΔT and when averaging preserves bias. This realism is documented in Supplementary Fig. S1, which collates 0 %, +5 %, and +50 % potentiometer-drift cases to one and two biased lanes.

2.5. Practical implications of equalisation techniques

By addressing the research gap, this study provides valuable insights into enhancing EMAs in modern aerospace applications, ensuring precise control over various aircraft and aerospace operations. Integrating equalisation techniques will significantly improve the efficiency and reliability of these systems while aligning with industry standards and DO-160 certifications [42]. Ultimately, this will deliver the substantial practical benefits outlined below.

- **Enhance Fault Tolerance and System Stability in Aerospace:** Although redundancy in EMAs enhances safety and reliability, parallel configurations can cause output inconsistencies, leading to load imbalances and mechanical risks. Equalisation improves fault tolerance, preserving system integrity even in the event of failure, ensuring greater stability and smoother responses.
- **Reduce Mechanical Stress and Prolonging Component Longevity:** Disproportionate torque distribution across actuators can strain critical components like gear systems and linkages, accelerating wear and increasing maintenance demands. Lane equalization minimizes localized stress by evenly distributing mechanical loads, extending component lifespan and reducing the likelihood of unexpected system failures.
- **Ensure Precision in Flight Control and Boosting Operational Efficiency:** EMAs are essential for controlling manoeuvring surfaces like ailerons, elevators, and rudders. Proper synchronization through lane equalisation ensures precise, uniform movement, enhancing aircraft handling and efficiency while reducing operational costs and increasing availability.

3. System under consideration

The study is based on four lanes of actuation that are designed to overcome (aerodynamic and inertial) loads on the inboard aileron control surface of the Sea Harrier aircraft.

The proposed T_Σ and V_Σ architectures were specifically designed to handle up to two failures, ensuring continued functionality under fault conditions [4,5,38]. To achieve this level of resilience, redundancy is incorporated into the motors and feedback transducers, allowing the system to maintain performance even in the presence of two failures. Each lane is equipped with a motor and microprocessor(s) to execute control and monitoring functions, further enhancing the system's robustness and reliability.

Fig. 7 summarises the end-to-end workflow, from system inputs and modelling, through equalisation and architecture choices, to simulation scenarios and outputs. Notation and assumptions are collated in Appendix A. Only the minimal equations required are repeated here.

Inputs include system and sensors (motors, potentiometers, tachometers) and operating modes/loads. Section 4 develops the model (loads, closed-loop control), represents inherent randomness, and defines equalisation strategies (F_{e_q}, L_{e_q}) with architecture selection ($T_\Sigma A, V_\Sigma A$). Section 5 runs the scenarios: inertial-load-dominant analysis and the effects of F_eq and L_eq on $T_\Sigma A$ *and* $V_\Sigma A$ under M_{nom} *and* $M_{T_{max\pm}}$ with FT_{nom} feedback, tachometer drift, and potentiometer drift. Outputs and metrics include lane-torque disparity ΔT, position/velocity tracking error, and stability or oscillation. Reporting uses one-sided predictive

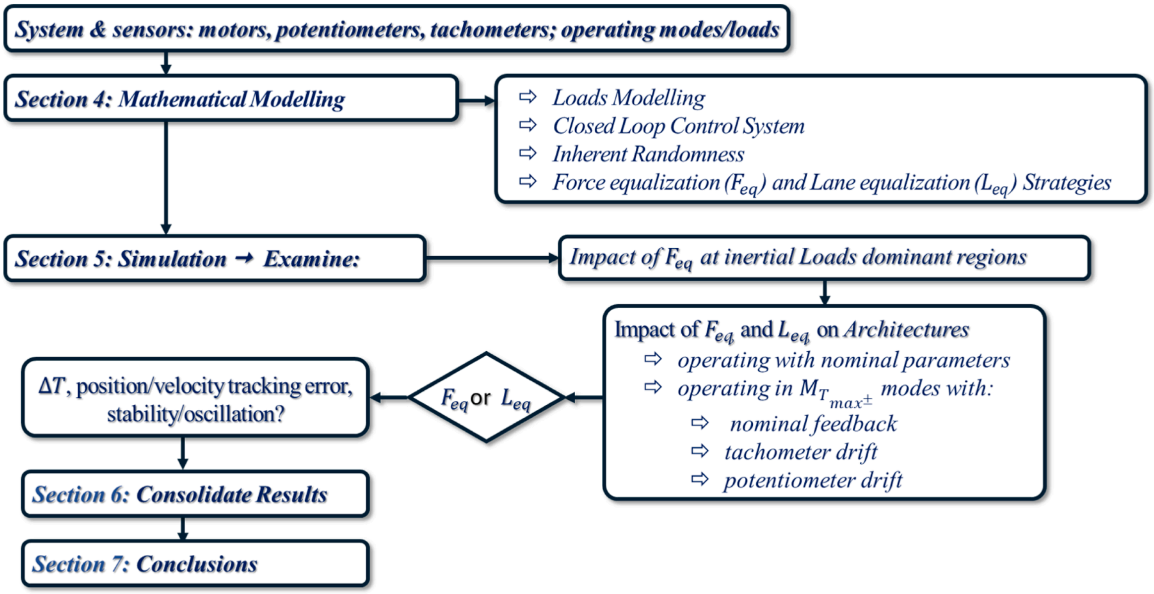

Fig. 7. Workflow of the proposed equalisation and evaluation method for multi-lane EMAs.

thresholds at $p = 0.9999$ (false alarm 10^{-4}), as defined in Section 2.4. Results are consolidated in Section 6 and summarised in Section 7.

In the T_ΣA architecture (Fig. 6), the resultant torque is the algebraic sum of the torques from the individual lanes. Although this configuration delivers high torque capability, it can lead to force-fight between mismatched active lanes. Equalisation, shown by the shaded blocks, reduces this force-fight.

Fig. 8 shows the V_ΣA architecture, where the common output shaft velocity or position is the average of the velocity (or position) contributions from the individual lanes. In this design, there is no concern about force fight between the active lanes. However, it is of interest to compare the effectiveness of F_{eq} in reducing lane disparities, particularly between inherently mismatched lanes that may have high tolerance variations or dormant drift in the feedback transducers.

In the V_Σ configuration, the output shaft speed is the average of the individual motor speeds, as shown in Fig. 8. Consequently, in this architecture, the placement of feedback sensors is irrelevant. In contrast, in the V_ΣA configuration, feedback sensor placement becomes important. Depending on cost and housing capacity, some designs may prioritize a combination of motor built-in and external transducers. However, regardless of the approach adopted, designs must comply with actuation and aircraft military standards [43,44]. In both architectures, the controllers in the equalisation approach utilized feedback signals based on the average measurements returned from the monitored

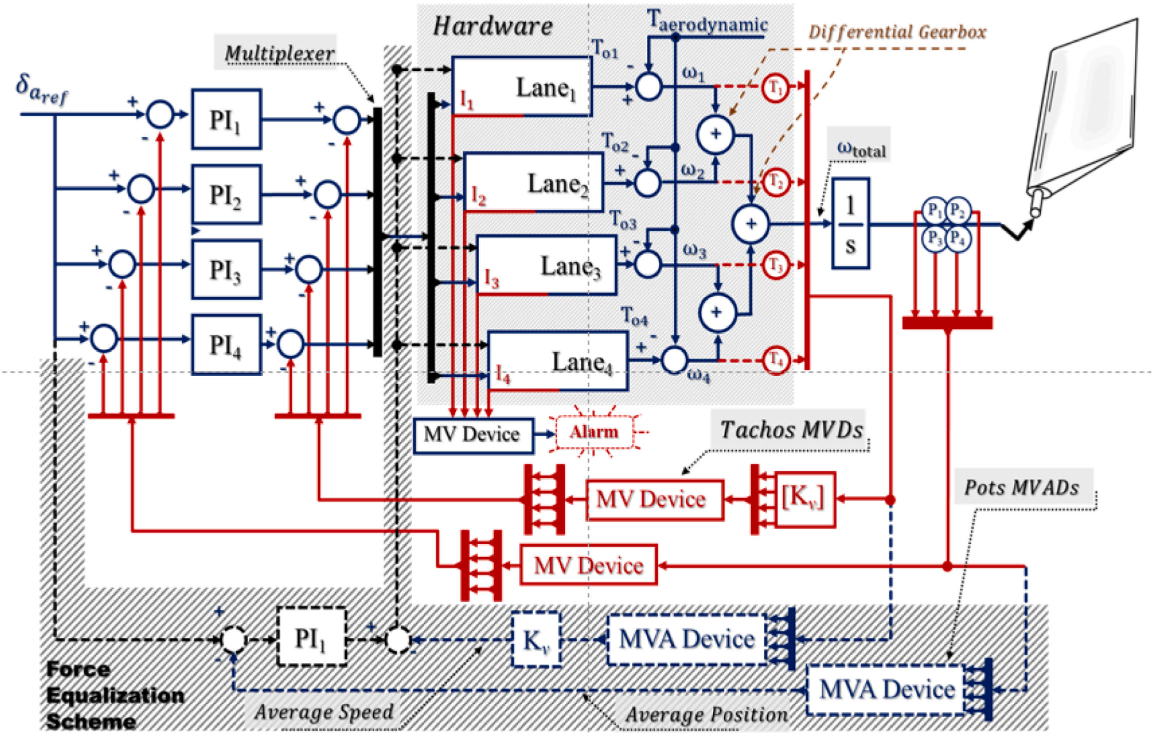

Fig. 8. V_Σ architecture with and without lane equalisation (L_{eq}) schemes; shaded blocks indicate the equalisation path.

redundant potentiometers and tachometers, processed through Monitoring-Voting-Averaging-Devices. However, when force equalisation is not considered (i.e., $\overline{F}_{eq}$), four independent position controllers drove each lane using independent position and velocity feedback signals. In this case, Monitoring-Voting-Devices were employed solely to monitor the potentiometers and tachometers for failure detection.

In assessing robustness to inherent lane mismatches and component tolerances, the effectiveness of equalisation in the V_Σ architecture is compared with the T_ΣA architecture. Fig. 8 shows the V_Σ architecture with and without lane equalisation (L_{eq}); Fig. 6 shows the T_ΣA architecture with and without force equalisation (F_{eq}). The shaded blocks in Figs. 6 and 8 indicate the equalisation injection points. The analysis uses simulations that contrast nominal parameters with cases exhibiting maximum lane-torque disparity (ΔT). Table 2 summarises the operating conditions and test cases (aerodynamic and inertial loads, and sensor-drift scenarios) considered for both architectures.

4. Mathematical modelling and equalisation architectures

This section defines the modelling framework for the torque-summed (T_Σ) and velocity-summed (V_Σ**)** architectures. The models comprise: (i) aerodynamic and inertial load models for the inboard aileron, (ii) a three-phase brushless-DC motor and drive representation that captures commutation and torque ripple [22], and (iii) a closed-loop control structure implemented in MATLAB/Simulink. Parameter spreads and sensor effects are included to represent inherent variability and slow drift, which create lane mismatch and occasional extreme torques. These elements are used to evaluate the equalisation strategies F_{eq} and L_{eq}, and to quantify lane-torque disparity ΔT and tracking error. Thresholds used for monitoring are defined in Section 2.4. Notation and assumptions (including e_ω, e_T, and the compact sharing laws) are collated in Appendix A. The detailed design of the fault-detection and isolation logic is outside the scope of this paper.

4.1. Load modelling

For both the T_Σ and V_Σ architectures, the impact of equalisation on reducing ΔT*s* will be assessed by considering closed-loop systems that include four-lane models driving aerodynamic and inertial load models. Each lane consists of three-phase motors and their associated switching circuit models. The inertial loads were shown to be proportional to the maximum sinusoidal authority limit excursions described by the aileron deflection, as the $\delta_a = \pm 18^o|_{M=0.2,\ 8Hz}$ flight case generates the maximum (inertial) loading [43]. The author in [45] demonstrated that the aerodynamic load consisted of variable (T_{A_v}) and a steady (T_{A_s}) components, as expressed in Eq. (1).

Table 2
Summary of working conditions used in simulations. This table summarises the aerodynamic, inertial, and sensor drift scenarios considered when evaluating torque-summed and velocity-summed EMA architectures.

Condition	**Values / Cases Considered**	**Purpose in Study**
Flight Speed (Mach, *M*)	0.2, 0.4, 0.5, 0.8 and 1.0	To capture different aerodynamic load scenarios
Aileron Deflection ($\boldsymbol{\delta_a}$, $\boldsymbol{^o}$)	$\pm 18^\circ$ at $M = 0.2 \sim 1.0$; and Deflections where aerodynamic load = 0. For example, at: • $\delta a \approx -9^\circ$ *at* $M = 0.2$ • $\delta a \approx -7^\circ$ *at* $M = 0.5$ • $\delta a \approx -3.5^\circ$ *at* $M = 0.8$	To simulate maximum inertial loading and zero-aero-load cases
Excitation Frequency (*f, Hz*)	8 Hz oscillation at low speed ($M = 0.2$)	To evaluate actuator response under dynamic excitation
Motor Torque Tolerance ($\boldsymbol{\Delta T}$, ***N.m***)	Extreme mismatch cases with two motors at $+T_{max}$, two at $-T_{max}$	To study force fight and lane disparities
Tachometer Drift (**%Δω**, ***deg*** */s*)	0 %, 50 % (single and double drift cases)	To evaluate impact of velocity feedback errors
Potentiometer Drift ($\boldsymbol{\Delta\theta_a}$, ***deg***)	0 %, 50 % (single and double drift cases)	To evaluate impact of position feedback errors

$$\begin{matrix}\text{Aerodynamic}\\ \text{load}\end{matrix} = \left[\overbrace{0.151791\ \alpha_{\mathrm{G}}}^{(\mathrm{T_{As}})} + \overbrace{4.3574\ \times 10^{-3}\ \delta_{\mathrm{a}}}^{(\mathrm{T_{Av}})}\right] \overline{\mathrm{Q}}(\mathrm{M})\dots\ \dots\ \dots \tag{1}$$

Where, ● T_{A_v} is aileron deflection and aircraft speed dependent; and

- T_{A_s} is aircraft speed dependant, thus, it remains constant on both aileron surfaces

The author in [45] demonstrated that the resultant load T_L, inertial load T_I, T_{A_v} and T_{A_s}were in the ranges: $240\text{Nm} \le T_L \le 5714\text{Nm}$, $10\text{Nm} \le T_I \le 5821\text{Nm}$, $219\text{Nm} \le T_{A_v} \le 1355\text{Nm}$, and $112\text{Nm} \le T_{A_s} \le 976\text{Nm}$, respectively. The influence of the inertial load is significant, becoming more dominant in regions where T_{A_v} completely cancels out T_{A_s}, as shown in Fig. 9a. This figure illustrates the distribution of resultant aerodynamic loads across various aircraft speeds for fixed δ_{a} (aileron deflection) and α_{G} values.

Although a comprehensive range of flight cases was analysed, the figure focuses on plotting the net aerodynamic loads for various aileron deflections at flight conditions of $M = 0.2$, 0.4, 0.5, and 0.8 flight cases. Therefore, the plotted loads correspond to the following aileron deflections: $\delta_{a|_{\pm 18^o, M=0.2}}$, $\delta_{a|_{\pm 14^o, M=0.4}}$, $\delta_{a|_{\pm 12^o, M=0.5}}$, *and* $\delta_{a|_{\pm 6^o, M=0.8}}$. *The figure shows* that the aerodynamic loads are reduced to Zero at specific aileron deflections, denoted as $\delta_{\not\approx}$. For example, $\delta_{\not\approx|_{M=0.2}} = \delta_{\not\approx|_{M=0.4}} = -9^0$; $\delta_{\not\approx|_{M=0.5}} \cong -7^0$; and $\delta_{\not\approx|_{M=0.8}} \cong -3.5^0$.

Fig. 9b expands on the cases of $\delta_{\not\approx|_{M=0.2}} = \pm 9^0$ and $\delta_{\not\approx|_{M=0.2}} = \pm 18^0$ cases. In this scenario, the reference inputs were initially set (over the period $0 \le t \le 0.25$) to examine the system's response to step inputs of $\pm 18^o$ *and* $\pm 9^o$ and then for $t \ge 0.25$, the reference inputs were modified by adding an 8 Hz sinusoidal variation with an amplitude of 0.5^o.

The net aerodynamic load clearly reduced to zero at $\delta_{\not\approx|_{M=0.2}} = -9^0$, before the reference input oscillated between -9.5^o and -8.5^o. Similar behaviour was observed for other reference angles, where the net aerodynamic load initially remained constant before beginning to oscillate at 8 Hz for $t \ge 0.25$ s.

Additionally, the perturbation size depended on the set reference input, and as expected, T_{A_s} contributed to the inertial load in one direction while opposing it in the other. Conversely, T_{A_v} consistently supported the inertial load in both directions, resulting in a slight imbalance as the aileron oscillated between the set reference inputs.

4.2. Closed-loop control system

Baseline controller. Position control uses a classical PID. In the non-equalised cases (Appendix B, Figs. B1 and B3), each lane has an independent PID position controller (identical gains cloned per lane). In the equalised cases (Appendix B, Figs. B2 and B4), a single outer PID position controller commands all lanes using averaged measurements from the healthy/active transducers. The same tuned gains are used across operating points and scenarios, and actuator/drive saturation limits are modelled. This enables a like-for-like comparison and isolates the contribution of the equalisation terms F_{eq} and L_{eq}.

The distinction between configurations is therefore in the command-sharing and monitoring topology: without equalisation, lanes are controlled independently from their own sensors; with equalisation, a common outer controller drives all lanes and the sharing terms F_{eq} (for T_Σ) or L_{eq} (for V_Σ) act on the lane commands to correct torque or speed sharing errors.

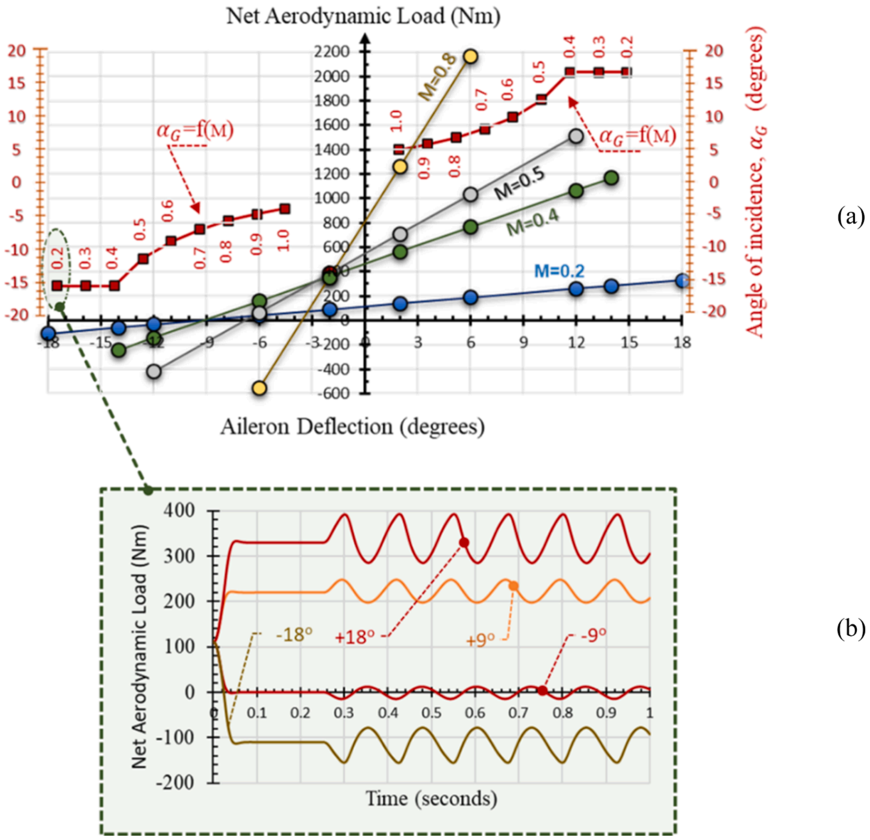

Fig. 9. Aerodynamic load distribution in relation to δ_a and M.

4.3. Inherent randomness

Repeatability in hardware does not imply that the hardware components (such as lanes or feedback transducers) are fully matched, as achieving 100 % identical parts is practically challenging. In this study, commercial motors and feedback transducers with high tolerances were considered, acknowledging the inherent mismatches between these components. The motors were assumed to have the following parameters: Resistances, $R = 7.2 \pm 12\%\ \Omega$; Inductance, $L = 17.7 \times 10^{-3} \pm 30\%\ H$; Torque Constant, $K_t = 1.0 \pm 10\%\ Nm/A$; and Voltage Constant, $K_v = 1.0 \pm 10\%\ V/rad/sec$. This resulted in motors operating at extreme torques ($T_{max^{\pm}}$), with two channels delivering $T_{max^{-}} = 9.43\ N.m$ and the other two channels delivering $T_{max^{+}} = 15.53\ N.m$ *[53]*.

Randomness in the sharing-error channels is represented by lumped disturbances $\delta_\omega(t)$ (velocity) and $\delta_T(t)$ (torque), which aggregate sensor noise/bias, lane-gain mismatch, load asymmetry and saturation effects. The corresponding error dynamics and symbols (e_ω, e_T) are summarised in Appendix A (A.2–A.4).

Additionally, the tolerances on feedback transducers were assumed to range between ±0.7 % and ±2.3 %, depending on the manufacturer [46–50]. These variances highlight the challenges posed by mismatched components in ensuring consistent performance across the system. The study initially considered feedback transducer tolerances of ±1 %. However, higher tolerances of up to 50 % were analysed to assess system performance under extreme conditions. These exaggerated drift assumptions were introduced to evaluate the potential impact of dormant or undetected transducer drift or failure on system response and the resulting ΔTs between lanes.

4.4. Equalisation strategies

Discrepancies between redundant actuation lanes can result in force fight, increased mechanical stress, and reduced control accuracy, necessitating robust equalisation strategies. In this study, two approaches are considered: Force Equalisation (F_{eq}) and Lane Equalisation (L_{eq}). Both methods aim to minimize inter-lane mismatches in torque-summed and velocity-summed electromechanical actuator architectures, thereby enhancing robustness and reliability.

Implementation details are provided in Appendix B (Figs. B1–B4); schematic placement of the equalisation terms appears in Fig. 6 (T_Σ) and Fig. 8 (V_Σ).

4.4.1. Force equalisation ($\boldsymbol{F_{eq}}$)

In this scheme, the equalisation signal is derived from the common output of the PID controller, which itself uses averaged position and velocity feedback processed through MVADs. This common control variable, U, is then distributed across all lanes. Where, mathematically, the individual contributions are the product of the generated individual currents and the lane's own torque constant, as shown in Eq. (2) below:

$$T_i = K_{t,i}.U\dots\ \dots\ \dots \quad (2)$$

where T_i is the torque of $Lane_i$ and $K_{t,i}$ is its motor torque constant. In this way, each lane tracks the same control demand but produces torques that depend on the mismatches in both torque constant and electrical parameters ($R_i, L_i, K_{e,i}$) and the total output driving torque is the sum of these individual torques multiplied by the implemented gearbox ratio. The total output driving torque is obtained by summing the contributions from all four lanes and multiplying by the gearbox ratio G, as shown in Eq. (3). This reduces the overall torque deviation, leading to balanced load sharing and suppression of force fight across the redundant actuation system.

$$T_{out} = G\sum_{1}^{4} T_i = G\sum_{1}^{4} K_{t,i}.U\dots\ \dots\ \dots \quad (3)$$

4.4.2. Lane equalisation (L_{eq})

While F_{eq} addresses torque mismatches directly at the actuator level, L_{eq} operates at the feedback signal level. Its objective is to suppress disparities in the position and velocity measurements among lanes, thereby limiting the propagation of sensor drift into control errors.

In this scheme, the feedback variables of the lanes (e.g., potentiometer position δ_{ai} or tachometer velocity ω_i) are compared through the MVAD system, returning which computes the average value of all healthy (or unisolated) devices, as shown in Eq. (4).

$$\overline{x} = \frac{1}{N_h} \sum_{i=1}^{N_h} x_i \ldots \ldots \ldots \tag{4}$$

where x_i is the feedback (position or velocity) signal of $Lane_i$, and N_h is the number of healthy (or unisolated) sensors. Each lane then uses these equalized or averaged $\overline{x}$ feedback signal. The scheme mitigates the effects of individual sensor drift or bias and reduces the potential damage caused by undetected drift.

4.5. Numerical simulation and tuning

Controller and equalisation gains were selected during the design stage using standard time and frequency domain criteria across the flight envelope (Mach M from 0 to 1) and authority limits representative of ground tests ($\delta_a = \pm 18^o$) tapering to $\delta_a = \pm 2^o$ at $M = 1$ [51]. Tests covered nominal operation and one- and two-fault cases (lane, potentiometer, tachometer), with loads exercised in both time and frequency domains [51]. Faults were introduced singly (no simultaneous initiations). Simulations used a single-rate, fixed-step discrete implementation in MATLAB/Simulink; all control and equalisation updates used the same sample time. Multi-rate scheduling and real-time scheduling constraints were not modelled.

Scope note. The simulations use a single-rate, fixed-step implementation in MATLAB/Simulink. The step size was chosen conservatively with respect to the fastest inner-loop dynamics and commutation ripple, and the same solver settings were applied in all scenarios and operating points. The models were exercised over a range of aircraft speeds and aileron deflections; to keep the presentation compact, results are reported for the worst-case operating point ($M = 0.2,\ \delta_a = \pm 18^o$) that produced the largest inertial loads. Given this operating-point sweep, an explicit step-size/gain sensitivity matrix would multiply the run set substantially and is therefore outside the scope of this paper; it is identified as future work.

To support replicability, the principal simulation parameters (PID gains, sampling time, drift magnitudes, and solver settings) are summarised in Table 3; these were held constant across all cases unless stated otherwise.

5. Simulation results

Results are presented in the order of the objectives: common framework and metrics, effects of mismatch and sensor bias and drift, architecture-specific behaviours, and design recommendations. This section then details the simulation results for the torque-summed and velocity-summed electromechanical actuator architectures introduced in Section 3 and modelled in Section 4. Results are organised by operating condition (nominal, mismatched, and drift-affected cases) and by the role of force equalisation and lane equalisation.

The analysis proceeds in three stages: first, the nominal system response with nominal motor parameters and nominal feedback transducers; second, the response under maximum torque mismatches; third, the influence of sensor drift (tachometer or potentiometer) with and without equalisation. Results are shown for the worst-case operating point ($M = 0.2,\ \delta_a = \pm 18^o$); other tested speeds and deflections exhibited the same qualitative trends.

Table 3
Working conditions and test cases used in the simulations.

Condition	**Setting (units)**	**Purpose in study**
Input command	Step, $\delta_{a\_ref} = \pm 18^o$	Excite transient response and steady-state tracking
Architecture	$T_\Sigma A$; $V_\Sigma A$	Compare torque-summed vs velocity-summed behaviours
Equalisation	F_{e_q} (on/off); L_{e_q} (on/off)	Assess impact on lane-torque sharing and tracking
Torque mismatch	$T_{max^-} = 9.43\ N.m$ $T_{max^+} = 15.53\ N.m$	Examine worst-case force-fight and lane disparity
Tachometer drift	0–50 % on $Tach_1$; 0–50 % on $Tach_1$ and $Tach_3$	Test sensitivity to biased velocity feedback
Potentiometer drift	0–50 % on Pot_1; 0–50 % on Pot_1 and Pot_3	Test sensitivity to biased position feedback
Aerodynamic load	331 $N.m$	Represent flight-relevant disturbance and loading
Controller	Baseline PID K_p=30; $K_i = 6s^{-1}$; K_d=1	Provide consistent control law across cases
Sampling time	$T_s = 1 \times 10^{-4}$ s	Ensure replicability and numerical stability
Simulation time	$T_{end} = 0.5–1$ s	Cover full transient and settling

5.1. Impact of force equalisation (F_{e_q}) at inertial-load-dominant regions

This subsection focuses on assessing the effect of F_{e_q} in systems with nominal parameters and load distributions in regions where the inertial loads are dominant. Fig. 10 illustrates the individual lane torques $(T_{q_{1\sim4}})$, total output torques (T_{Total}), and the aileron angular deflections for the $\pm 9^o|_{M=0.2}$ and $\pm 18^o|_{M=0.2}$ flight cases. In this case study, it is evident that all lanes responded in a similar manner (with the individual lane responses being superimposed on each other). As a result, the torque disparities (ΔTs) for all cases are equal to zero. Consequently, F_{e_q} had no significant effect on the response for systems operating with nominal parameters.

Figs. 10a and 10b clearly show that the developed torques at regions where the inertial load are dominant (referred to as δ_Z angles) are merely mirrored reflections of those at the $-\delta_Z$ angles. Thus, uncontrolled fluttering maybe dismissed, and load distributions around these regions are not considered a limitation and will not be included in further discussions.

5.2. Further analysis of F_{e_q} on $T_\Sigma A$ and L_{e_q} on $V_\Sigma A$

Both architectures use identical controller and equalisation parameters so that trends in behaviour can be compared directly, rather than absolute performance. The analysis focuses on the low-speed, high-inertia case at $M = 0.2$ with maximum control-surface authority $\delta_a = 18^o|_{M=0.2}$, which produces the largest inertial loads on the inboard aileron. Results are reported in terms of lane-torque disparity ΔT(Nm), position/velocity tracking error, and qualitative stability or oscillation notes.

Exact responses were obtained for the velocity-summed architecture ($V_\Sigma A$).

5.3. F_{e_q} on $T_\Sigma A$ and $V_\Sigma A$ with M_{nom} and FT_{nom}

Figs. 11a and 11b present the responses of the T_Σ and V_Σ architectures under nominal parameters. As expected, irrespective of the equalisation schemes, identical responses were observed for each architecture. The plots highlight performance differences between the two architectures and provide a reference framework for the analyses that follow in Section 5 and the discussion in Section 6.

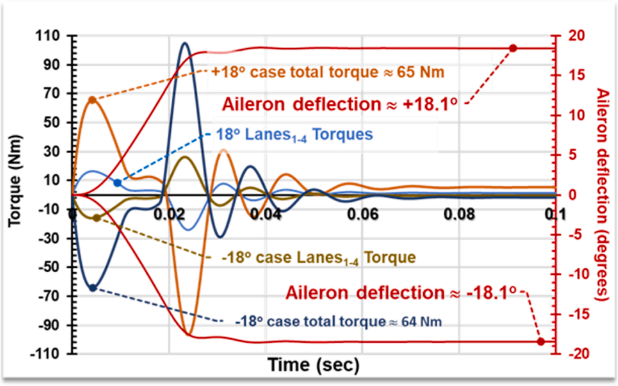

(a) $\pm 18^o$ input: Responses show accurate position tracking with negligible lane torque disparities.

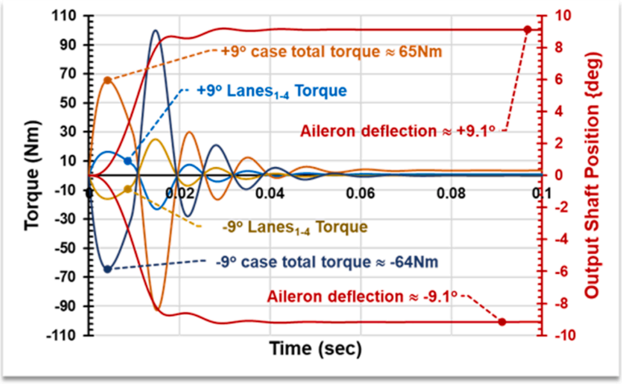

(b) $\pm 9^o$ input: Responses show accurate position tracking with negligible lane torque disparities.

Fig. 10. Torque-summed architecture ($T_\Sigma A$) response under nominal conditions with M_{nom} and FT_{nom}.

5.4. $\boldsymbol{F_{e_{\not q}}}$ on $\boldsymbol{T_\Sigma A}$ and $\boldsymbol{V_\Sigma A}$ with $\boldsymbol{M_{T_{max^\pm}}}$ and $\boldsymbol{FT_{nom}}$

The effect in both T_Σ and V_Σ architectures will be examined further by analysing configurations in which motors operate at $T_{max^\pm}$ ($\boldsymbol{M_{T_{max^\pm}}}$) limits with nominal, drift free feedback transducers (FT_{nom}). In this $\boldsymbol{M_{T_{max^\pm}}}$ scenario, $Motors_{1\&2}$ produce equal torques of $T_{q_1} = T_{q_2} = T_{max^+}$, while $Motors_{3\&4}$ produce equal torques of $T_{q_3} = T_{q_4} = T_{max^-}$. This isolates equalisation effects from transducer drift. Figs. 12 and 13 show the responses under $T_{max^\pm}$ and FT_{nom} at low aircraft speed and $+18^o$ aileron input.

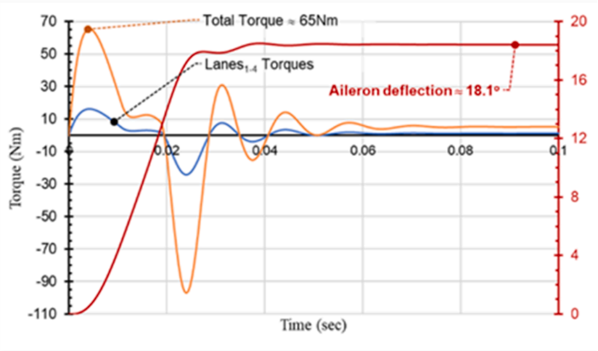

(a) $T_\Sigma A$: Responses demonstrate accurate position tracking with significant disparities in lane torque contributions.

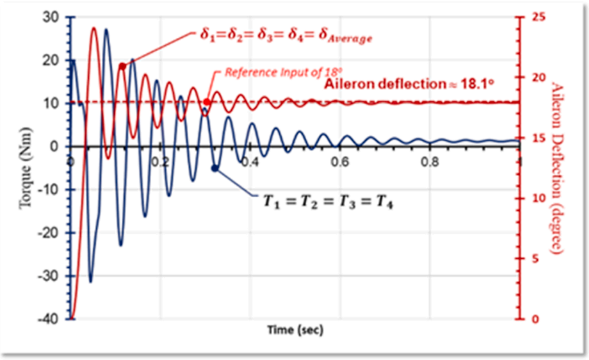

(b) $V_\Sigma A$: Responses demonstrate accurate position tracking with lane torques remaining equal (no lane-to-lane disparities).

Fig. 11. Responses under M_{nom} and FT_{nom}; ±18° input.
(a) $T_\Sigma A$: Responses demonstrate accurate position tracking with significant disparities in lane torque contributions.
(b) $V_\Sigma A$: Responses demonstrate accurate position tracking with lane torques remaining equal (no lane-to-lane disparities).

5.4.1. *Considering the* $\mathbf{T_{\Sigma}A}$

Fig. 12 shows the $T_{\Sigma}A$ system response with and without F_{e_q}. In both schemes, the motors were operating in the $T_{max^{\pm}}$ mode and the feedback transducers are not experiencing any drift. Fig. 12a shows that with F_{e_q}, the system response closely resembles that of Fig. 11a, albeit with a slight increase in the overall ΔTs. However, the disparities between mismatched lanes remain constant, and the torque disparities (ΔT) between similar channels remain zero throughout the response (i.e., $\Delta T_{13} = \Delta T_{23} = \Delta T_{14} = \Delta T_{24}$ and $\Delta T_{12} = \Delta T_{34} = 0$).

Conversely, as shown in Fig. 12b, when F_{e_q} is not applied, the torque disparities between lanes become more pronounced (i.e., $T_{q_{1\&2}} \neq T_{q_{3\&4}}$, yet $\Delta T_{12} = \Delta T_{34} = 0$ and $\Delta T_{13} = \Delta T_{14}$, $\Delta T_{23} = \Delta T_{24}$). This outcome aligns with expectations, as the absence of transducer drift eliminates additional variables influencing the response.

These observations lead to the conclusion that F_{e_q} does not significantly impact the actuator's response in the $T_{\Sigma}A$ architecture, and the actuator ultimately settled at 18.4°, irrespective of the equalisation scheme.

5.4.2. *Considering the* $\mathbf{V_{\Sigma}A}$

Fig. 13 presents the $V_{\Sigma}A$ system responses with and without lane equalisation (L_{e_q}). In both configurations, the motors operate in $T_{max^{\pm}}$ mode, and the feedback transducers are assumed to be free from drift. The results clearly demonstrate that in both L_{e_q} and $\overline{L}_{e_q}$ (with and without lane equalisation) schemes, matched lanes delivered similar outputs ($\delta_1 = \delta_2$ and $\delta_3 = \delta_4$). Additionally, it is evident that the contributions of these pairs to the final output shaft differ, highlighting the unique dynamics of the $V_{\Sigma}A$ architecture. These observations suggest that the implementation of L_{e_q} does not disrupt the inherent pairing consistency of matched lanes but may influence how each pair contributes to the overall system performance.

Figures show that L_{e_q} does not disrupt the inherent pairing consistency of matched lanes but influences how each pair contributes to the overall system performance.

In the L_{e_q} scheme, Lanes 1 and 2 and Lanes 3 and 4 contribute approximately 20° and 16°, respectively, leading to a steady final average rotation of 18° Conversely, in the $\overline{L}_{e_q}$ scheme, the contributions from the pairs were equal but fluctuating, resulting in an output that oscillates around the 18° set value. These findings indicate that equalisation was effective in both the T_{Σ} and V_{Σ} architectures, ensuring improved system stability and performance.

Building on these results, the next subsection (5.5) extends the analysis to cases where the architectures operate in $T_{max^{\pm}}$ modes while experiencing tachometer drift, in order to assess the robustness of equalisation under biased velocity feedback.

5.5. $\boldsymbol{F_{e_q}}$ *on* $\mathbf{T_{\Sigma}A}$ *and* $\mathbf{V_{\Sigma}A}$ *with* $\boldsymbol{M_{T_{max^{\pm}}}}$ *and* $\boldsymbol{T_{drift}}$

As in section 5.4, the effect of equalisation on disparity for the T_{Σ} and V_{Σ} architectures, but under configurations where the motors operate at $T_{max^{\pm}}$ with drift in their tachometer readings. Although several drift magnitudes across different flight cases were analysed, this section focuses on the low-aircraft-speed scenario with a maximum authority limit of 18°, incorporating tachometer drifts of 50 % in one and two readings. In the single-drift case, the drift occurs on the tachometer in $lane_1$ (i.e., $Tacho_1$). In the two-drift scenario, the drifts are applied to the tachometers in $lanes_{1\&3}$ (i.e., $Tacho_{1\&3}$), where Lanes 1 and 3 are assumed to deliver torques of $T_{max^{+}}$ and $T_{max^{-}}$, respectively.

Figs. 14 and 15 summarise the system responses under tachometer drift for both $T_{\Sigma}A$ and $V_{\Sigma}A$. The results compare cases with and without equalisation, highlighting the ability of F_{e_q} to reduce torque disparities in $T_{\Sigma}A$ and the limited effect of L_{e_q} in $V_{\Sigma}A$, where lane torques remain inherently balanced. These figures provide a basis for examining how equalisation influences system stability and accuracy under biased velocity feedback.

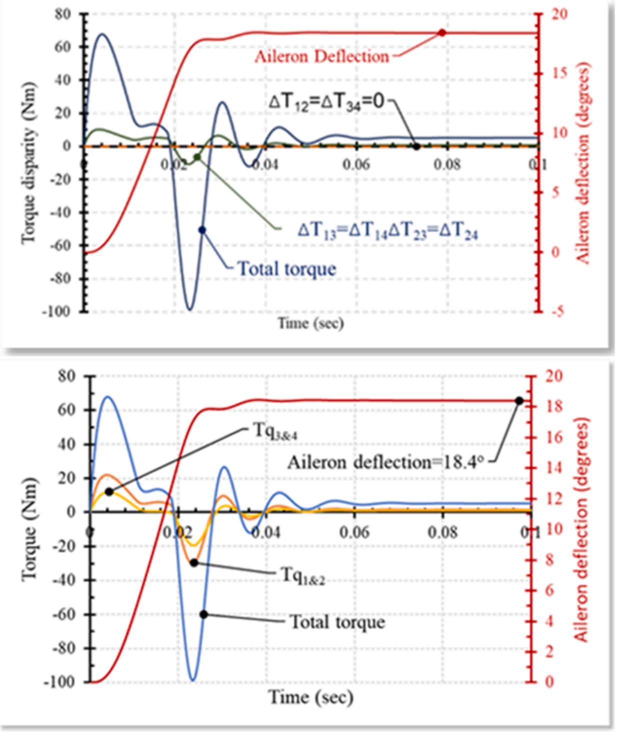

(a) With F_{e_q}: Responses show accurate position tracking with reduced lane torque disparities compared to the unequalised case.

(b) Without F_{e_q}: Responses show accurate position tracking but with significant disparities in lane torque contributions.

Fig. 12. Impact of force equalisation (F_{e_q}) on the torque-summed architecture ($\mathscr{T}_{\Sigma}A$) operating under maximum torque motor mismatches ($T_{max^{\pm}}$) with nominal feedback readings (FT_{nom}) and $+18^{o}$ input. Lane-torque disparity ΔT is reported in Nm.
(a) With F_{e_q}: Responses show accurate position tracking with reduced lane torque disparities compared to the unequalised case.
(b) Without F_{e_q}: Responses show accurate position tracking but with significant disparities in lane torque contributions.

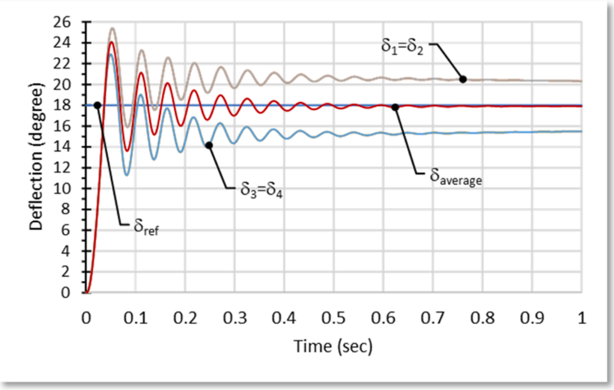

(a) With L_{e_q}: Responses remain unchanged, confirming that lane torques stay equal and pairing consistency is preserved under zero-drift conditions.

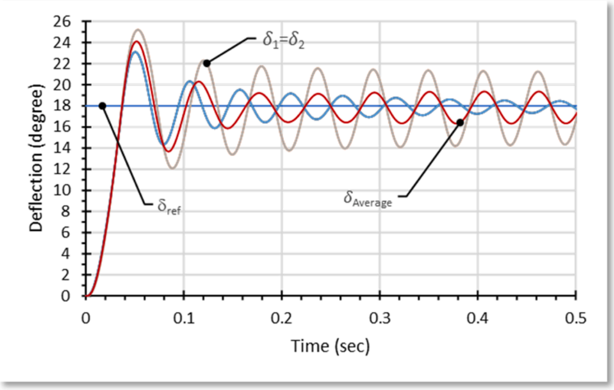

(b) Without L_{e_q}: Responses show accurate position tracking with lane torques remaining equal across all lanes.

Fig. 13. Impact of lane equalisation (L_{e_q}) on the velocity-summed architecture ($V_{\Sigma}A$) operating under maximum torque motor mismatches ($T_{max^{\pm}}$) with nominal feedback readings (FT_{nom}) and $+18^{o}$ input.

(a) With L_{e_q}: Responses remain unchanged, confirming that lane torques stay equal and pairing consistency is preserved under zero-drift conditions.

(b) Without L_{e_q}: Responses show accurate position tracking with lane torques remaining equal across all lanes.

5.5.1. Considering the $\boldsymbol{T_{\Sigma}}$ *architecture*

Figs. 14a, 14b and 14c illustrate the system's response to the flight case, with and without the application of F_{e_q}. Figs. 14a shows the system response of the F_{e_q} architecture. The response is irrespective of the drift magnitude in the tachometer channel readings.

Figs. 14b and 14c are of the responses in the absence of equalisation. Although they may appear similar at first glance, a closer examination uncovers significant differences. Fig. 14b shows that there are noticeable torque disparities between $lanes_1$ and the other lanes. Although these disparities gradually diminish over time due to the lanes being mechanically locked together, the reduction occurs at the cost of added strain on the gearbox teeth, potentially compromising the system's durability. The torque disparities are even more pronounced in Fig. 14c, where the system experiences drift in the tachometer readings for $lanes_{1\&3}$.

This highlights the adverse effects of feedback inaccuracies and underscores the importance of F_{e_q} in mitigating these disparities and reducing mechanical stress within the T_{Σ} architecture.

5.5.2. Considering the $\boldsymbol{V_{\Sigma}A}$ *architecture*

Fig. 15 illustrates the system's response with and without lane equalisation (L_{e_q} and $\overline{L}_{e_q}$) to the $18^{o}|_{M=0.2}$ flight case. Fig. 15a displays the individual lane contributions and the overall average system response with L_{e_q}, regardless of the level of drift affecting one or more tachometers. This response mirrors that shown in Fig. 13a, and it is repeated here to underscore the effect of the absence of L_{e_q}. Here, it was assumed that $lanes_{1\&2}$ and $lanes_{3\&4}$ are operating at $T_{max^{\pm}}$. Consequently, the two-lane pairs displace the load by 20° and 16°, respectively, to collectively meet the overall set demand of 18° This highlights the balancing role of L_{e_q} in ensuring stable contributions from the paired lanes, even in the presence of drift, maintaining the system's ability to meet its operational requirements effectively.

Fig. 15c, 15d, and 15e depict the responses for the architecture without lane equalisation ($\overline{L}_{e_q}$). Regardless of the degree of drift in tachometer readings or the number of affected lanes, lane-torque disparities decay slowly, producing an oscillatory response about the 18° demand.

Fig. 15b demonstrates how L_{e_q} (regardless of amount of drift) torque disparities across all lanes are reduced to zero, unlike the responses in Fig. 15f, where torque disparities remain across lanes are not reduced to zero.

These observations highlight the pivotal role of equalisation in reducing lane disparities within both T_{Σ} and V_{Σ} architectures. Therefore, equalisation is instrumental in delivering a stable output and a more balanced and reliable system response, even under diverse conditions and operational challenges.

The following subsection (5.6) extends this investigation to potentiometer drift, examining how F_{e_q} and L_{e_q} influence system behaviour when position feedback signals are biased.

5.6. $\boldsymbol{L_{e_q}}$ *on* $\boldsymbol{T_{\Sigma}A}$ *and* $\boldsymbol{V_{\Sigma}A}$ *with* $\boldsymbol{M_{T_{max^{\pm}}}}$ *and* $\boldsymbol{P_{drift}}$

This section examines the impact of equalisation in the T_{Σ} and V_{Σ} architectures with the motors operating at the torque limits ($T_{max^{\pm}}$) under potentiometer drift. Figs. 16–17 compare responses with and without equalisation, highlighting the influence of L_{e_q} on system robustness.

While various degrees of drift across different flight cases were analysed, this section highlights the scenario of low aircraft speed with a maximum authority limit of 18°, incorporating 50 % drift in one and two potentiometer readings. In the single-drift case, the drift is applied to the potentiometer in $lane_1$ (i.e., Pot_1), whereas in the two-drift scenario, the

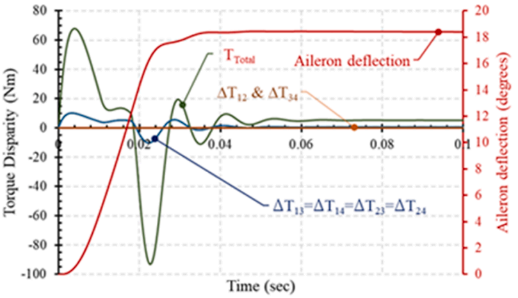

(a) 0% drift: Responses show accurate position tracking with reduced lane torque disparities compared to the unequalised case.

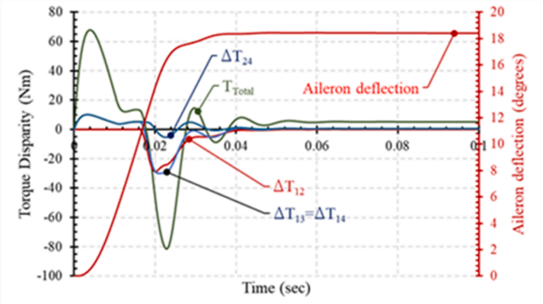

(b) 50% drift on $Tach_1$ without F_{eq} $(\bar{F}_{eq})$: Responses show increased torque disparities and degraded velocity feedback.

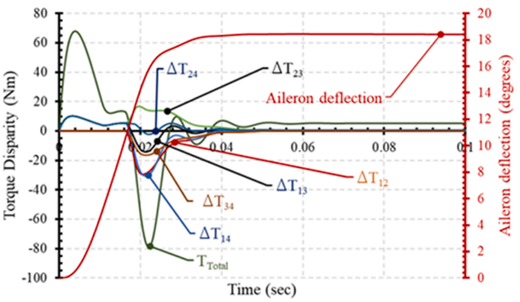

(c) 50% drift on $Tach_{1,3}$ without F_{eq} $(\bar{F}_{eq})$: Responses show more severe torque disparities, further stressing the system.

Fig. 14. Impact of force equalisation (F_{e_q}) on the torque-summed architecture ($T_{\Sigma}A$) operating under maximum torque motor mismatches ($T_{max^{\pm}}$) with and without tachometer drift, and $+18^o$ input.
(a) 0 % drift: Responses show accurate position tracking with reduced lane torque disparities compared to the unequalised case.
(b) 50 % drift on $Tach_1$ without F_{e_q} ($\bar{F}_{e_q}$): Responses show increased torque disparities and degraded velocity feedback.
(c) 50 % drift on $Tach_{1,3}$ without F_{e_q} ($\bar{F}_{e_q}$): Responses show more severe torque disparities, further stressing the system.

drifts are applied to the potentiometers in $lane_{1\&3}$ (i.e., $Pot_{1\&3}$). Here, Lanes 1 and 3 are assumed to deliver torques of deliver torques of T_{max^+} and T_{max^-}, respectively.

Supplementary Fig. S1 gathers 0 %, +5 %, and +50 % potentiometer-drift variants (one and two biased lanes) to provide baseline, realistic, and stress-test context alongside Figs. 16–17.

The primary objective of this analysis is to investigate the impact of potentiometer drift on the contributions of individual lanes and to assess the effectiveness of equalisation in mitigating these disparities within the T_{Σ} and V_{Σ} architectures.

5.6.1. *Considering the* $\mathbf{T_{\Sigma}}$ *architecture*

The impact of F_{e_q} on torque disparities was evaluated under conditions of single potentiometer drift in Pot_1 or double potentiometer drift in $Pots_{1\&3}$. The plots in Fig. 16 depict the system response for the $18^o|_{M=0.2}$ flight case with the motors operating in the $T_{max^{\pm}}$ modes.

Fig. 16a depicts the system response without any potentiometer drift, resembling the responses previously shown in Figs. 10a, 11a, and 14a. In the F_{e_q} architecture, the responses shown in Fig. 16b and 16c, corresponding to the actuator experiencing 50 % drift in Pot_1 and $Pots_{1\&3}$, respectively, are remarkably similar to the response depicted in Fig. 16a. This consistency demonstrates the robustness of F_{e_q} in maintaining stable actuator performance despite significant potentiometer drift.

In contrast, when F_{e_q} is not applied (Figs. 16d and 16e), there is a substantial increase in torque disparities as the actuator encounters drift in its potentiometer readings. For the system with 50 % drift in Pot_1 (Fig. 16d), the overall desired response is still achieved, however, the torque disparities are significantly more pronounced. This issue is exacerbated in the case of 50 % drift in $Pots_{1\&3}$ (Fig. 16e), where the disparities intensify, resulting in a further degradation of the overall system response. This demonstrates the robustness of F_{e_q} in maintaining consistent system performance, even in the presence of significant drift.

5.6.2. *Considering the* $\mathbf{V_{\Sigma}}$ *architecture*

The plots in Fig. 17 illustrate the impact of L_{e_q} on actuator responses under various degrees of drift in Pot_1 and $Pots_{1\&3}$ readings. Fig. 17a shows the actuator response without drift on any of the potentiometer readings. Thus, the responses resemble those that were presented earlier in Figs. 13a and 15a. The figures clearly show that actuator output ($\delta_{average}$) settles at the set demand input of 18°.

The remaining plots in Fig. 17 depict the actuator responses under potentiometer drift conditions. Figs. 17b and 17c show the responses with L_{e_q}, corresponding to 50 % drift in Pot_1 and 50 % drift in $Pots_{1\&3}$, respectively. Conversely, Figs. 16e and 16f illustrate the responses without L_{e_q} for the same drift scenarios.

These comparisons highlight the fact that while L_{e_q} was effective in producing a stable output, it also introduced notable errors. For a reference command of 18°, the actuator could only deliver outputs of 16° and 14° when the potentiometers on $Lane_1$ *and* $Lanes_{1\&3}$ experienced drift, respectively. Fig. 17d demonstrates how L_{e_q} (regardless of amount of drift) torque disparities across all lanes are reduced to zero,

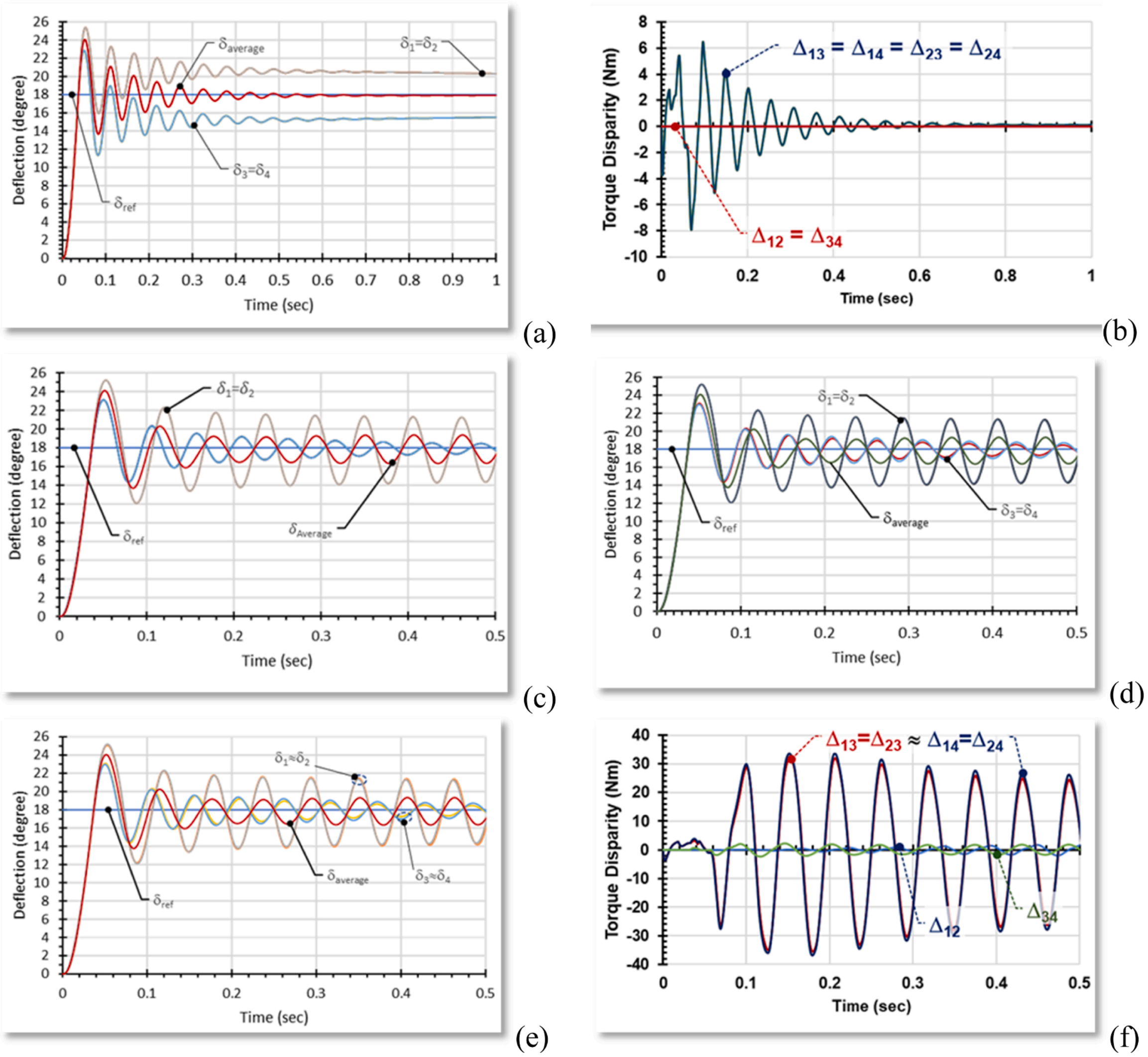

Fig. 15. Impact of lane equalisation (L_{e_γ}) on the velocity-summed architecture ($V_\Sigma A$) operating under maximum torque motor mismatches ($T_{max^\pm}$), with and without tachometer drift, and $+18^o$ input.
(a) Regardless of amount of drift with L_{e_γ}: Responses show accurate position tracking with ΔTs remaining equal across all lanes.
(b) Torque disparities with L_{e_γ}: Regardless of amount of drift ΔTs are reduced to zero.(c) 0 % drift without L_{e_γ}: Responses show accurate position tracking with lane torques remaining equal across all lanes.(d) 50 % drift on $Tach_1$ without L_{e_γ}: Responses show biased average velocity feedback and degraded tracking.
(e) 50 % drift on $Tach_{1,3}$ without L_{e_γ}: Responses show multiple drift effects compounding, further degrading system performance.
(f) ΔTs under 50 % drift on $Tach_{1,3}$ without L_{e_γ}: Torques are not reduced to zero.

unlike the responses in *Fig. 15g*, where torque disparities across all lanes remain and are not reduced to zero.

This degraded performance is notably better than the scenario where lane equalisation was not implemented. In such cases (and as depicted in the plots of Figs. 17e and 17f) the actuator produced oscillatory outputs around the degraded outputs. This contrast in response is summarised in Fig. 18.

Responses show that lane torques remain equal across all lanes, while potentiometer bias introduces steady-state errors in the averaged output deflection.

Fig. 19 further clarifies the reason behind the degraded performance in the output. It illustrates the actual and measured contributions of individual lanes, along with the total output, when equalisation was implemented. Fig. 19a demonstrates how $Lanes_{2\sim4}$ slow down to compensate for the 50 % drift in Pot_1. As a result, the measured actuator output aligns with the set demand value of 18°, while the actual output is only 16°. This discrepancy arises because the 50 % increase in Pot_1 readings cause a corresponding reduction in the contributions from the remaining lanes to maintain the set reference input of 18°. Consequently, although the measured output matches the set value, the actual physical output falls short, leading to degraded performance.

A similar effect takes place when the actuator experiences a 50 % drift in $lanes_{1\&3}$, as shown in Figure19b. In this scenario, the 50 % increase in the measurements of $Pot_{1\&3}$ is accompanied by a proportional decrease in the outputs of $Lanes_{2\&4}$. This results in a further reduction of the overall output, bringing it down to 14°. These results demonstrate how drift in potentiometer readings affects the system's ability to deliver accurate physical outputs, despite the measured values meeting the set demand, underscoring the challenges posed by such drifts even with equalisation implemented.

While F_{e_γ} was effective in reducing lane disparities caused by potentiometer drift in the T_Σ architecture, L_{e_γ} led to degraded steady-state performance in the V_Σ architecture. This difference can be attributed to the fundamental distinctions between the two architectures. In the V_Σ architecture, velocity summing allows for torque alignment between the mismatched lanes, without any restriction. This inherently leads to larger lane disparities that can cause individual lanes to exhibit runaway contributions, that results in further degrading performance.

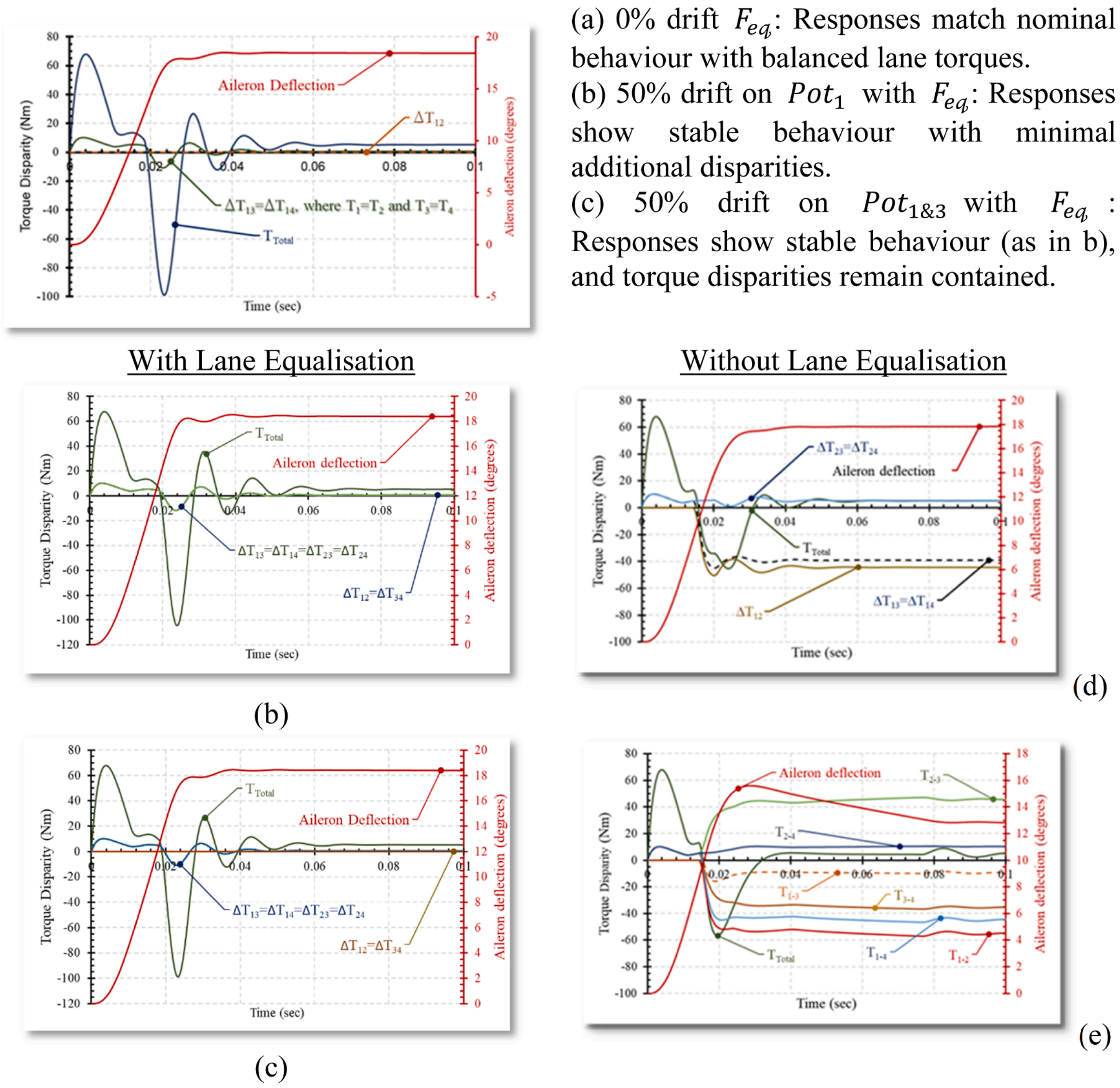

(a) 0% drift F_{e_q}: Responses match nominal behaviour with balanced lane torques.

(b) 50% drift on Pot_1 with F_{e_q}: Responses show stable behaviour with minimal additional disparities.

(c) 50% drift on $Pot_{1\&3}$ with F_{e_q} : Responses show stable behaviour (as in b), and torque disparities remain contained.

With Lane Equalisation

Without Lane Equalisation

(b)

(c)

(d)

(e)

Fig. 16. Impact of force equalisation (F_{e_q}) on the torque-summed architecture ($T_{\Sigma}A$) operating under maximum torque motor mismatches ($T_{max^{\pm}}$) with and without potentiometer drift, and $+18^{o}$ input.(a) 0 % drift F_{e_q}: Responses match nominal behaviour with balanced lane torques.(b) 50 % drift on Pot_1 with F_{e_q}: Responses show stable behaviour with minimal additional disparities.(c) 50 % drift on $Pot_{1\&3}$ with F_{e_q}: Responses show stable behaviour (as in b), and torque disparities remain contained.(d) 50 % drift on Pot_1 without F_{e_q}: Responses show increased torque disparities and reduced accuracy.(e) 50 % drift on $Pot_{1\&3}$ without F_{e_q}: Responses show increased torque disparities and degrading overall system response.

Fig. 20 highlights the key differences in torque disparity reduction between the T_{Σ} and V_{Σ} architectures. In the case of a 50 % drift on Pot_1, the disparities between $Lanes_{1\&2}$ diminish more rapidly to zero in the V_{Σ} architecture than in the T_{Σ} architecture (i.e., $\Delta T_{12} = 0$). This faster reduction occurs because the V_{Σ} configuration allows for quicker lane equalisation. However, this comes at the cost of higher disparities with the other lanes (i.e., $\Delta T_{13} = \Delta T_{14} = \Delta T_{23} = \Delta T_{24}$).

Responses show F_{e_q} reduces ΔT in $T_{\Sigma}A$, while $V_{\Sigma}A$ maintains equal lane torques but exhibits a biased averaged output. (In all cases $\Delta T_{12} = \Delta T_{34} = 0$; and $= \Delta T_{13} = \Delta T_{14} = \Delta T_{23} = \Delta T_{24}$)

A similar effect is observed in the 50 % drift on $Pots_{1\&3}$. In this scenario, torque disparities between $Lanes_{1\&2}$ and $Lanes_{3\&4}$ (i.e., $\Delta T_{12} = \Delta T_{34} = 0$) reduce more rapidly in the V_{Σ} architecture compared to the T_{Σ} architecture. However, this again leads to higher disparities with the other lanes ($\Delta T_{13} = \Delta T_{14} = \Delta T_{23} = \Delta T_{24}$).

Sections 5.4–5.6 characterise the effects under of equalisation under tachometer and potentiometer drift for $T_{\Sigma}A$ and $V_{\Sigma}A$. In $T_{\Sigma}A$, F_{e_q} consistently reduces lane-torque disparity. By contrast, in $V_{\Sigma}A$, L_{e_q} has limited influence because lane torques are inherently balanced, although biased feedback degrades tracking accuracy. Section 5.7 synthesises these findings to provide a consolidated perspective across both architectures and drift conditions.

5.7. *Consolidated results for drift and equalisation across architectures*

This subsection synthesises observations from Sections 5.4–5.6 on the respective effects of F_{e_q} and L_{e_q} on the T_{Σ} and V_{Σ} architectures under the following conditions: Zero-drift (FT_{nom}) with $T_{max^{\pm}}$, Tachometer drift (T_{drift}) with $T_{max^{\pm}}$, and Potentiometer drift (P_{drift}) with $T_{max^{\pm}}$. Figs. 11–17 provide the supporting results. All results are interpreted against one-sided predictive thresholds at $p = 0.9999$ (false alarm 10^{-4}), as defined in Section 2.4.

5.7.1. *Zero-drift with* $\boldsymbol{T_{max^{\pm}}}$

For $T_{\Sigma}A$, lane-torque disparities are evident under $T_{max^{\pm}}$; applying F_{e_q} reduces ΔT while preserving accurate position-tracking (Fig. 12). For $V_{\Sigma}A$, with unbiased sensors and matched parameters, the control law drives all lanes to the same speed using a common command and

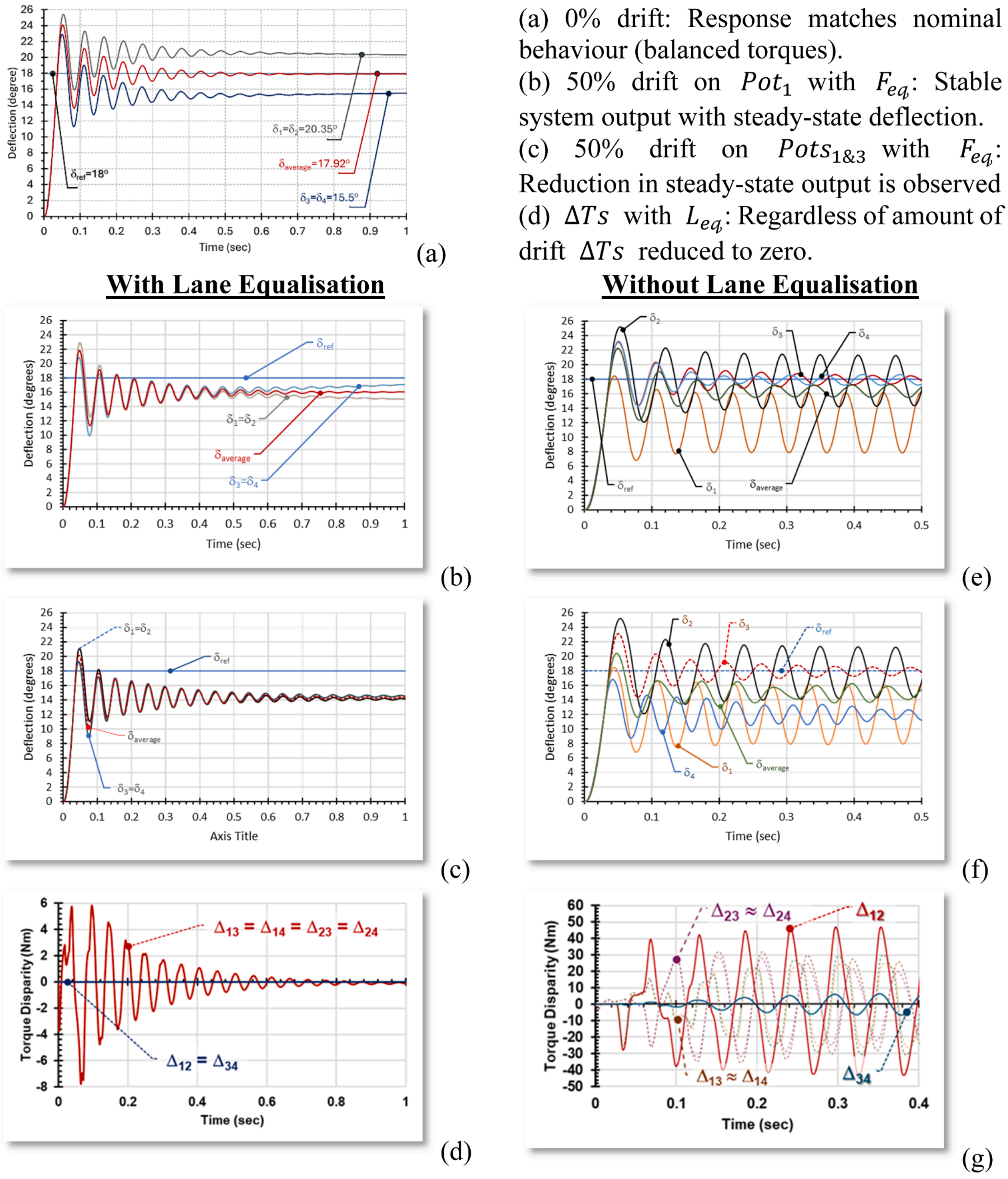

(a) 0% drift: Response matches nominal behaviour (balanced torques).
(b) 50% drift on Pot_1 with F_{eq}: Stable system output with steady-state deflection.
(c) 50% drift on $Pots_{1\&3}$ with F_{eq}: Reduction in steady-state output is observed
(d) ΔTs with L_{eq}: Regardless of amount of drift ΔTs reduced to zero.

Fig. 17. Impact of L_{eq} on the velocity-summed architecture ($V_{\Sigma}A$) in $T_{max^{\pm}}$ mode, with potentiometer drift.(a) 0 % drift: Response matches nominal behaviour (balanced torques).(b) 50 % drift on Pot_1 with L_{eq}: Stable system output with steady-state deflection.(c) 50 % drift on $Pots_{1\&3}$ with L_{eq}: Reduction in steady-state output is observed.
(d) ΔTs with L_{eq}: Regardless of amount of drift ΔTs reduced to zero.(e) 50 % drift on Pot_1 without L_{eq}: Oscillatory responses around a degraded output.(f) 50 % drift on $Pots_{1\&3}$ without L_{eq}: Oscillatory response, with further degraded output.
(g) ΔTs under 50 % drift on $Pot_{1,3}$ without L_{eq}: Torques are not reduced to zero.

averaged feedback; this makes lane torques equal in steady state, so applying L_{eq} produces no torque disparities (Fig. 13).

5.7.2. Tachometer drift

In $T_{\Sigma}A$, velocity-feedback errors increase lane-torque mismatches and excite oscillatory behaviour; F_{eq} mitigates ΔT but residual velocity-tracking error remains (Fig. 14). In $V_{\Sigma}A$, lane torques remain equal, but the averaged velocity feedback becomes biased; L_{eq} reduces the bias impact on the averaged signal by reducing lane torque differences, though overall velocity tracking is degraded (Fig. 15).

5.7.3. Potentiometer drift

In $T_{\Sigma}A$, potentiometer bias introduces steady-state offsets in output deflection; F_{eq} reduces lane-torque disparities but cannot remove the steady-state offset (Fig. 16). In $V_{\Sigma}A$, lane torques remain equal and L_{eq} has limited effect on the steady-state position error introduced by biased position feedback (Fig. 17).

At-a-glance parallel view: the qualitative effects of equalisation across architectures and scenarios are summarised in Table 4. These consolidated results provide the basis for the interpretive discussion and implications developed in Section 6.

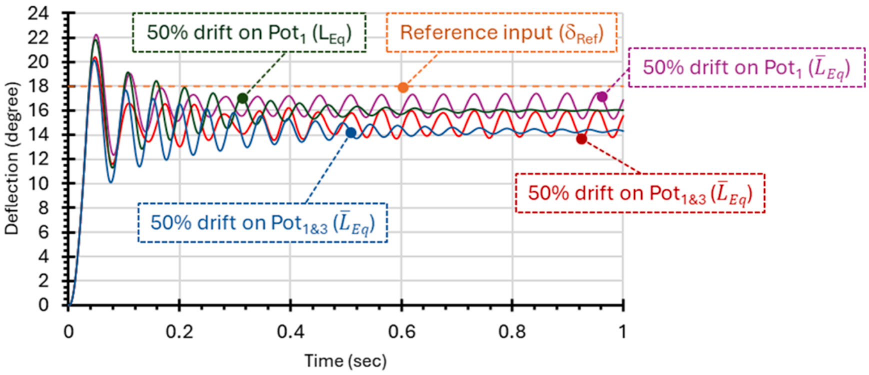

Fig. 18. Impact of lane equalisation (L_{e_q}) on the velocity-summed architecture ($V_\Sigma A$) under potentiometer drift with $T_{max^\pm}$. and $+18^o$ input.

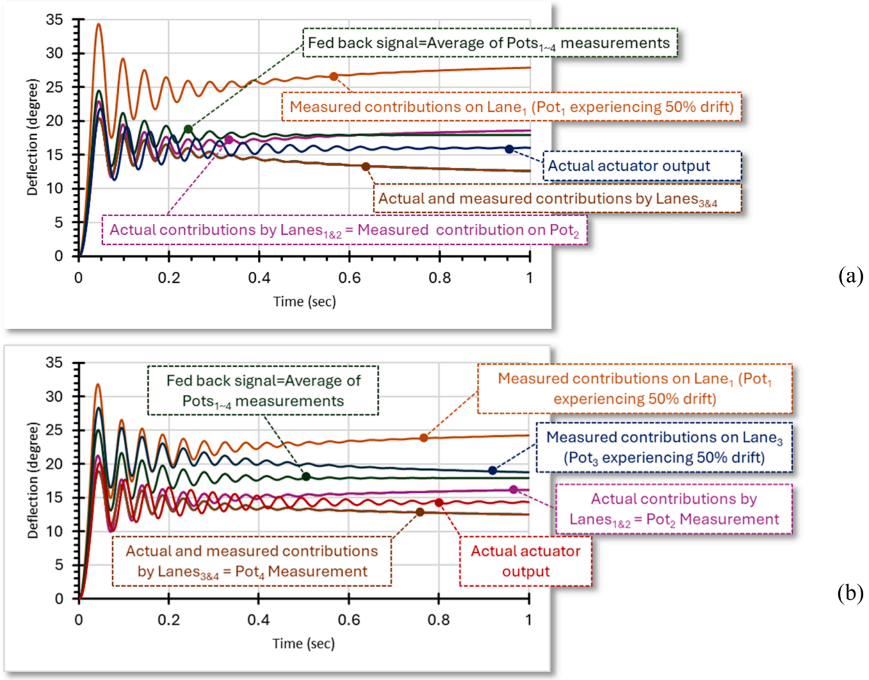

Fig. 19. Comparison of actual and measured responses under potentiometer drift with L_{e_q} equalisation applied in $V_\Sigma A$, and $T_{max^\pm}$ and $+18^o$ input. The plots illustrate individual lane and total actuator response, and the effect of biased feedback on the averaged signal.(a) 50 % drift on Pot_1; (b) 50 % drift on $Pots_{1\&3}$.

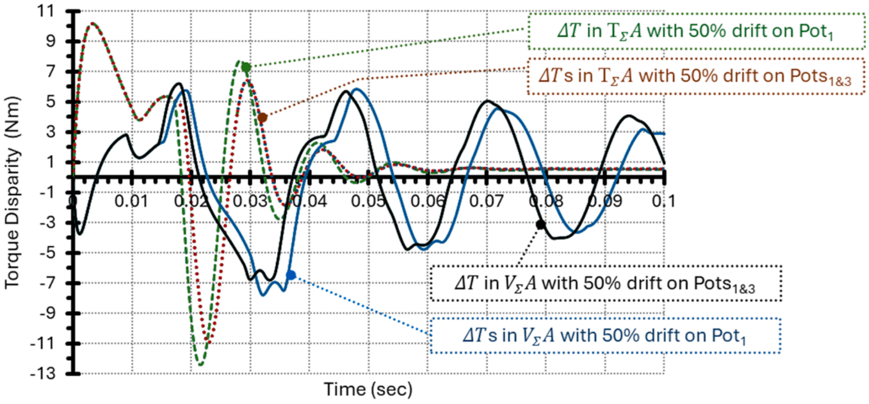

Fig. 20. Torque disparities in the torque-summed ($T_\Sigma A$) and velocity-summed ($V_\Sigma A$) architectures under potentiometer drift with $T_{max^\pm}$ and $+18^o$ input.

6. Discussion

This section interprets the simulation results presented in Section 5 and situates them within the wider context of electromechanical actuator design for all-electric aircraft. Rather than restating results, it explains the observed behaviours, compares the relative effectiveness of equalisation schemes, and highlights implications for system robustness and reliability. In particular, it examines trade-offs between torque-summed (T_Σ) and velocity-summed (V_Σ) architectures, and the limitations of force equalisation $\left(F_{eq}\right)$ and lane equalisation (L_{eq}) under sensor drift. Predictive thresholds used in this study correspond to a false-alarm probability of 10^{-4} ($p = 0.9999$), as defined in Section 2.4.

6.1. *Comparative insights*

The results demonstrate that torque-summed architectures benefit directly from F_{eq}, which reduces lane-torque disparities and mitigates the mechanical stress associated with mismatched actuators. By contrast, velocity-summed architectures inherently maintain equal lane torques, so that L_{eq} offers limited additional benefit. However, the averaging of biased signals in $V_\Sigma A$ introduces steady-state errors that remain uncorrected by equalisation. $V_\Sigma A$

6.2. *Impact of drift*

Under tachometer drift, $T_\Sigma A$ experiences velocity-feedback errors that propagate into the control loop, increasing torque disparities and oscillatory behaviour. Although F_{eq} reduces the severity of these disparities, residual errors persist. For $V_\Sigma A$, tachometer drift corrupts the averaged velocity signal, leading to degraded tracking accuracy despite equal lane torques. Under potentiometer drift, $T_\Sigma A$ exhibits steady-state offsets that are not eliminated by F_{eq}, while $V_\Sigma A$ continues to show equal lane torques but suffers from biased position feedback and corresponding output errors.

In both architectures, potentiometer bias enters as a steady-state offset in the outer loop; equalisation cannot remove a constant bias because it averages biased measurements. Practical mitigations include explicit bias estimation or adaptive observers and sensor redundancy with voting to exclude biased channels. For tachometer drift, the bias contaminates the velocity feedback within the inner loop; equalisation cannot remove it. Mitigations include augmented-state bias observers on the speed signal, cross-lane residual checks with redundant tachometers, or periodic re-trim during zero-rate conditions.

Supplementary Fig. S1 gathers 0 %, +5 %, and +50 % potentiometer-drift cases (one and two biased lanes) to illustrate baseline, realistic, and stress-test behaviour consistent with these mechanisms.

Table 4
Qualitative effects of equalisation across architectures and drift scenarios, operating at $\boldsymbol{T_{max^{\pm}}}$ with a step command $\boldsymbol{\delta_{ref}} = 18^o$. $\boldsymbol{\Delta T}$ in Nm.

		T_Σ		V_Σ	
		Without F_{eq}	**With F_{eq}**	**Without L_{eq}**	**With L_{eq}**
Zero drift	*ΔT*	*Noticeable*	*Reduced*	≈ 0	≈ 0
	Tracking	*Good*	*Maintained*	*Good*	*Maintained*
Tacho drift	*ΔT*	*Amplified*	*Reduced*	≈ 0	≈ 0
	Tracking	*Degraded*	*Improved*	*Oscillatory; lanes diverge*	*Oscillatory; less diverge*
Pot drift	*ΔT*	Increased	Contained	Contained	Contained
	Tracking	*Degraded*	*Maintained.*	*Degraded*	*Further degraded*

Notes: $\boldsymbol{T_\Sigma A}$ = torque-summed architecture; $\boldsymbol{V_\Sigma A}$ = velocity-summed architecture; $\boldsymbol{F_{eq}}$ = force equalisation; $\boldsymbol{L_{eq}}$ =lane equalisation; $\boldsymbol{\Delta T}$ = lane-torque disparity; $\boldsymbol{\delta_{ref}}$ = reference deflection. “Contained” = disparity bounded within the no-drift range; “≈ 0” = within numerical tolerance.

Takeaway: $\boldsymbol{T_\Sigma}$ benefits materially from $\boldsymbol{F_{eq}}$ in reducing $\boldsymbol{\Delta T}$, but remains sensitive to biased feedback. $\boldsymbol{V_\Sigma}$ is robust in torque sharing by construction; $\boldsymbol{L_{eq}}$ brings little additional benefit under drift, and biases appear primarily as tracking error.

6.3. *Computational considerations*

Runtime or latency were not quantified in this study. The equalisation and cross-monitoring terms are closed-form, non-iterative algebraic evaluations performed once per sample in the single-rate, fixed-step discrete-time model. Actual overhead depends on the target platform and sampling rate; practical implementations should include timing checks and, if necessary, distribute computations across lanes or adjust monitoring frequency. As detailed in Section 4.5, all control and equalisation updates used the same sample time in a single-rate, fixed-step implementation; full timing/latency benchmarking and hardware-in-the-loop validation are left to future work.

6.4. *Strengths and limitations*

The study provides the first systematic comparison of $T_\Sigma A$ and $V_\Sigma A$ under realistic non-idealities such as torque ripple, sensor drift, and lane mismatches. To evidence realism without expanding the main figures, Supplementary Fig. S1 gathers 0 %, +5 %, and +50 % potentiometer-drift cases to one and two biased lanes, confirming the same qualitative trends: in $T_\Sigma A$, F_{eq} reduces lane-torque disparity ΔT; in $V_\Sigma A$, torque sharing remains inherently balanced and L_{eq} has limited influence on ΔT while the tracking bias reflects the applied offset.

A limitation of the present work is the reliance on PID control and simulation-based results. Frequency-domain robustness analysis, hardware-in-the-loop validation, and exploration of advanced control strategies (e.g., adaptive or model-predictive control) remain as future extensions. Furthermore, cyber-physical vulnerabilities, such as spoofing of feedback channels, were not examined here but represent a critical avenue for future research. Computational overhead and latency were not measured; implementation-specific timing on the target platform is left to future work. A comprehensive numerical-stability sensitivity (step size and gain perturbations) and real-time/HIL benchmarking are beyond the present scope and are left to future work (see Section 4.5).

For realism, Supplementary Fig. S1 collates 0 %, +5 %, and +50 % potentiometer-drift cases, which are consistent with these mechanisms and conclusions.

6.5. *Implications*

The comparative evaluation of F_{eq} and L_{eq} provides evidence-based guidance for the design of multi-lane redundant electromechanical actuators in safety-critical systems. Torque-summed architectures, when combined with robust equalisation, offer resilience to motor mismatches and drift but remain sensitive to sensor bias. Velocity-summed architectures eliminate inter-lane torque disparities but are vulnerable to biased feedback, limiting reliability under drift conditions. These implications are synthesised into recommendations in Section 7.

6.6. *Advanced controllers*

To isolate the effects of architecture and equalisation, a single PID position controller was used across all scenarios (see Section 4.2). Under saturation and drift the PID exhibits the expected performance degradation reported in Section 5. More advanced designs, such as sliding-mode control for robustness to matched uncertainties, model predictive control for explicit constraint handling and optimisation, and adaptive gain scheduling for time-varying dynamics, could further improve margins. A structured evaluation and comparison of these controllers is beyond the present scope and is identified as future work.

7. Conclusions

This paper has advanced the understanding of lane equalisation in four-lane electromechanical actuators operating with significantly mismatched lanes. Two architectures were analysed: torque-summed and velocity-summed. Both were designed to withstand inertial and aerodynamic loads, including scenarios with two motor failures. The analysis also considered regions dominated by inertial loading (negligible aerodynamic loading), mitigating concerns about flutter instabilities under those conditions.

The comparative evaluation of F_{eq} and L_{eq} yielded the following key findings:

Effectiveness of Equalisation: Equalisation effectively reduced torque disparities in both architectures under mismatched motor conditions, including cases with drift in one or two tachometers.

Limitations with Drift in Potentiometers: In $T_\Sigma A$, equalisation maintained stable performance despite single or multiple potentiometer drifts. In $V_\Sigma A$, equalisation preserved lane balance but introduced steady-state errors in the averaged output signal.

Overall, these results demonstrate the potential of equalisation to enhance the robustness and stability of multi-lane EMAs in safety-critical aerospace applications. Torque-summed architectures, when supported by force equalisation, provide resilience to mismatches and sensor drift, whereas velocity-summed architectures maintain balanced lane torques but remain vulnerable to biased feedback signals.

By addressing mismatches and sensor drift through robust equalisation strategies, this study advances the reliability of all-electric actuation systems and supports the broader transition toward safer, more efficient, fully electrified aircraft architectures.

It would be valuable to extend the analysis through hardware-in-the-loop validation and to develop adaptive equalisation strategies to strengthen resilience under operational conditions. Promising directions include model-predictive control to anticipate drift, adaptive observers to estimate and correct biased feedback, and machine-learning-based methods to identify and compensate for nonlinearities in real time.

Fig. 1. The two proposed electromechanical architectures
Fig. 2. Early consolidation mechanizations that dealt with mismatched inputs
Fig. 3. Servo-hydraulic actuator and electromechanical actuator hybrid systems
Fig. 4. Control system schematic of test bench [29]
Fig. 5. Redundant actuation system with adaptive control [36]
Fig. 6. T_Σ architectures with and without force equalisation (F_{eq}) schemes [22]
Fig. 7. Workflow of the proposed equalisation and evaluation method for multi-lane EMAs.
Fig. 8. V_Σ architecture with and without lane equalisation (L_{eq}) schemes
Fig. 9. Aerodynamic load distribution in relation to δ_a and M
Fig. 10. Torque-summed architecture ($T_\Sigma A$) response under nominal conditions with M_{nom} and FT_{nom}. The exact responses were also obtained for the velocity-summed architecture ($V_\Sigma A$).
Fig. 11. Responses under maximum torque mismatches ($M_{T_{max^\pm}}$) with FT_{nom}; $\pm 18^o$ input.
Fig. 12. Impact of force equalisation (F_{eq}) on the torque-summed architecture ($\mathscr{T}_\Sigma A$) operating under maximum torque motor mismatches ($T_{max^\pm}$) with nominal feedback readings (FT_{nom}) and a $+18^o$ input.
Fig. 13. Impact of lane equalisation (L_{eq}) on the velocity-summed architecture ($V_\Sigma A$) operating under maximum torque motor mismatches ($T_{max^\pm}$) with nominal feedback readings (FT_{nom}) and a $+18^o$ input.
Fig. 14. Impact of force equalisation (F_{eq}) on the torque-summed architecture ($T_\Sigma A$) operating under maximum torque motor mismatches ($T_{max^\pm}$) with and without tachometer drift, and a $+18^o$ input.
Fig. 15. Impact of lane equalisation (L_{eq}) on the velocity-summed architecture ($V_\Sigma A$) operating under maximum torque motor mismatches ($T_{max^\pm}$), with and without tachometer drift, and a $+18^o$ input.
Fig. 16. Impact of force equalisation (F_{eq}) on the torque-summed architecture ($T_\Sigma A$) operating under maximum torque motor mismatches ($T_{max^\pm}$) with and without potentiometer drift, and a $+18^o$ input.
Fig. 17. Impact of L_{eq} on the velocity-summed architecture ($V_\Sigma A$) in $T_{max^\pm}$ mode, with potentiometer drift.
Fig. 18. Impact of lane equalisation (L_{eq}) on the velocity-summed architecture ($V_\Sigma A$) under potentiometer drift with $T_{max^\pm}$. and a $+18^o$ input.
Fig. 19. Comparison of actual and measured responses under potentiometer drift with L_{eq} equalisation applied in $V_\Sigma A$, and $T_{max^\pm}$ and a $+18^o$ input.
Fig. 20. Torque disparities in the torque-summed ($T_\Sigma A$) and velocity-summed ($V_\Sigma A$) architectures under potentiometer drift with $T_{max^\pm}$ and a $+18^o$ input.
Fig. B1. T_Σ closed-loop block diagram without F_{eq}.
Fig. B2. T_Σ closed-loop block diagram with F_{eq}.
Fig. B3. V_Σ closed-loop block diagram without L_{eq}.
Fig. B4. V_Σ closed-loop block diagram with L_{eq}.

CRediT authorship contribution statement

Fawaz Y Annaz: Writing – review & editing, Writing – original draft, Visualization, Validation, Supervision, Resources, Methodology, Investigation, Funding acquisition, Formal analysis, Data curation, Conceptualization.

Declaration of competing interest

The authors declare that they have no known competing financial interests or personal relationships that could have appeared to influence the work reported in this paper.

Supplementary materials

Supplementary material associated with this article can be found, in the online version, at doi:10.1016/j.ast.2025.111129.

Appendix A. Equalisation architectures, notation, and supporting details

A.1 Scope and notation

The deterministic plant, commutation and torque-ripple background follow the established actuator formulations in Annaz [45]. Equalisation and monitoring concepts follow Annaz [5]. Only the symbols required for this study are listed below.

A.2 Velocity-summed ($\boldsymbol{V}_{\boldsymbol{\Sigma}}$) and Torque-summed ($\boldsymbol{T}_{\boldsymbol{\Sigma}}$) architectures

For two lanes with common reference ω_{ref}:

- **Velocity-summed, $\boldsymbol{V}_{\boldsymbol{\Sigma}}$**

$$\omega_{1,cmd} = \omega_c - \frac{1}{2}K_{eq}(\omega_1 - \omega_2)\dots\dots\dots \tag{A.1}$$

$$\omega_{2,cmd} = \omega_c + \frac{1}{2}K_{eq}(\omega_1 - \omega_2)\dots\dots\dots \tag{A.2}$$

Equalisation-error dynamic (velocity channel)

$$\frac{d(e_\omega)}{dt} = -k_{eq}\, e_\omega + \delta_\omega(t), e_\omega = \omega_1 - \omega_2\dots\dots\dots \tag{A.3}$$

- **Torque-summed, $\boldsymbol{T}_{\boldsymbol{\Sigma}}$**

$$T_{1,cmd} = T_c - \frac{1}{2}K_{sh}(T_1 - T_2)\dots\dots\dots \tag{A.4}$$

$$T_{2,cmd} = T_c + \frac{1}{2}K_{sh}(T_1 - T_2)\dots\dots\dots \tag{A.5}$$

Equalisation-error dynamic (torque channel)

$$\frac{d(e_T)}{dt} = -k_{sh}\cdot e_T + \delta_T(t), e_T = T_1 - T_2\dots\dots\dots \tag{A.6}$$

Here, $\delta_\omega(t)$ and $\delta_T(t)$ are lumped disturbances that aggregate sensor noise/bias, lane-gain-mismatch, load-torque imbalance, unmodelled effects, and saturation.

A.3 Randomness and disturbances used in simulation

- Measurement noise: Additive noise on potentiometer and tachometer channels.
- Drift: Slowly varying bias added to the affected channel (tachometer or potentiometer) over the scenario duration.
- Lane mismatch: Small multiplicative spreads in lane parameters that create torque disparity.
- Torque ripple and commutation effects: These are treated as periodic disturbances as in Annaz [45].

A.4 Monitored channels and threshold definition

Motors, potentiometers and tachometers are monitored for faults. Thresholds are one-sided predictive quantiles set to a false-alarm probability of 10^{-4} ($p = 0.9999$) as defined in Section 2.4 and motivated by Annaz ([5], Fig. 9; Sections 11–13).

A.5 Symbols used in the paper (Table A1)

Symbol	Meaning	Units	Note
J	Load inertia	$kg\cdot m^2$	As used in Section 4
B	Viscous damping	$N.m\cdot s\cdot rad^{-1}$	
$\boldsymbol{K_{eq}}$ and $\boldsymbol{K_{sh}}$	Equalisation gains (in velocity and Torque channels); scales the per-lane correction from the mismatch in the command law.		V_Σ and T_Σ
$\boldsymbol{k_{eq}}$ and $\boldsymbol{k_{sh}}$	Effective closed-loop decay rate of the (speed and torque) sharing errors		V_Σ and T_Σ
$\boldsymbol{e_\omega}$	Velocity disparity ($\omega_1 - \omega_2$)	$rad\cdot s^{-1}$	
$\boldsymbol{e_T}$	Torque disparity ($T_1 - T_2$)	$N.m$	Appears as ΔT in figures
$\boldsymbol{\delta_\omega(t)}$	Lumped disturbance in velocity-disparity channel	$rad\cdot s^{-2}$	Sensor bias/noise, mismatch, load asymmetry, saturation
$\boldsymbol{\delta_T(t)}$	Lumped disturbance in torque-disparity channel	$N.m\cdot s^{-1}$	As in $\delta_\omega(t)$, mapped to torque
Pot	Angular displacement measurements	rad	
Tach	Angular speed measurements	$rad.s^{-1}$	
P	Predictive quantile level	—	$p = 0.9999$

A.6 Assumptions and validity

Inner loops are linear around the operating point. Delays and cross-coupling are small. Under strong non-linearities such as backlash, dominant Coulomb friction or hard PWM saturation, the simplified error models in A.2 may not hold. Results remain empirically valid but mechanistic interpretation should be cautious.

Appendix B. Detailed Simulink block diagrams and implementation notes

Figures

Sections

Notes. These diagrams complement the simplified schematics in Fig. 6 ($\boldsymbol{T_\Sigma}$) and Fig. 8 ($\boldsymbol{V_\Sigma}$). All blocks use the fixed sample time specified in Section 4.5; no multi-rate scheduling is applied.

Table B1
Symbols for Appendix B.5–B.6.

Symbol	**Meaning**
$\boldsymbol{i}$	Lane index ($i = 1\ldots N$)
$\boldsymbol{N_h}$	Number of healthy or active lanes used for averaging
$\boldsymbol{\theta_i}$	Position measurement in $lane_i$
$\boldsymbol{\omega_i}$	Speed measurement in $lane_i$
$\boldsymbol{\bar{\theta}},\boldsymbol{\bar{\omega}}$	Averaged position and speed over healthy lanes
$\boldsymbol{r_i^\theta}$, $\boldsymbol{r_i^\omega}$	Residuals for $lane_i$ (deviation from average)
$\boldsymbol{r_{max}^\theta},\boldsymbol{r_{max}^\omega}$	Maximum residual across lanes
$\boldsymbol{q_p}$	Predictive threshold at exceedance probability p (e.g., $p = 0.9999 = q_{0.9999}$)
$\boldsymbol{p}$	False-alarm probability used for thresholding
$\boldsymbol{e_T}$ **or** $\boldsymbol{e_\omega}$	Torque and speed sharing errors
$\boldsymbol{F_{eq}}$ or $\boldsymbol{L_{eq}}$	Force or Lane equalisation terms applied to lane commands
$\boldsymbol{u_i}$	Command to $lane_i$ (e.g., torque or speed command)
$\boldsymbol{h_i}$	Health flag for $lane_i$ (1 = healthy, 0 = faulted)
$\boldsymbol{m_i}$	Enable mask for $lane_i$ (1 = enabled, 0 = disabled)

B.1 $\boldsymbol{T_\Sigma}$ closed-loop block diagram without $\boldsymbol{F_{eq}}$

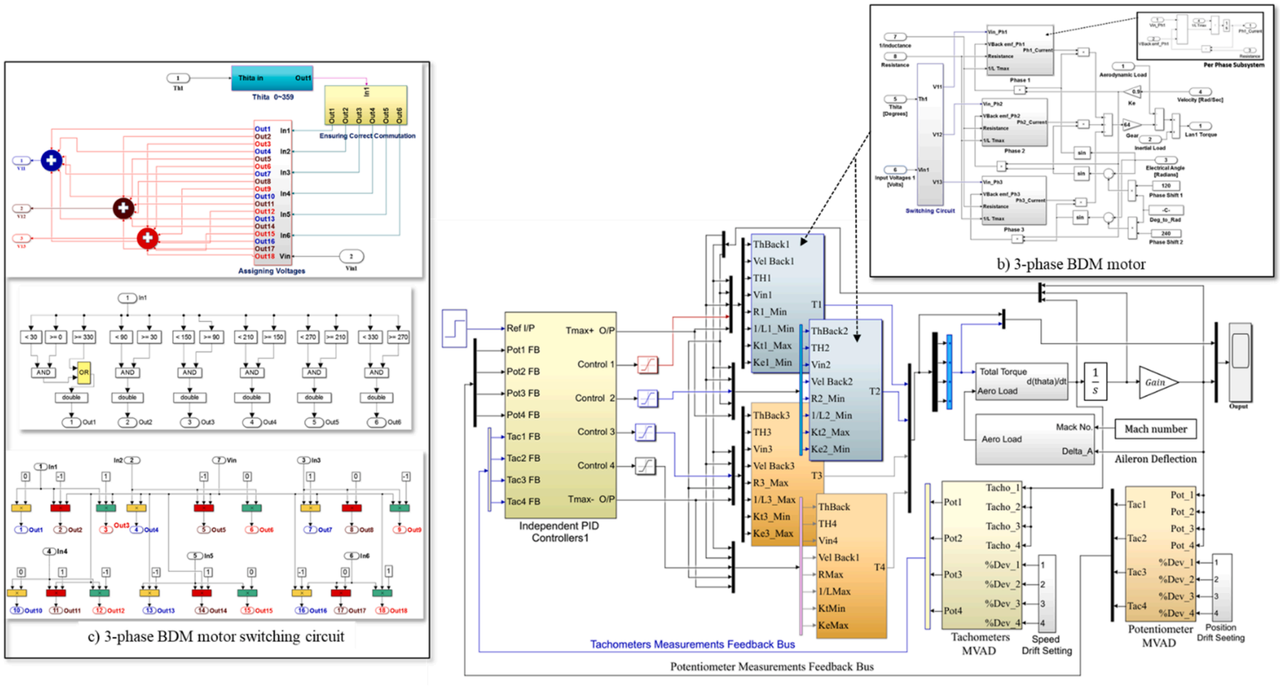

b) 3-phase BDM motor

c) 3-phase BDM motor switching circuit

a) Closed loop block diagram of the system with force-equalization

Fig. B1. T_Σ closed-loop block diagram without F_{eq}.

B.2 $\boldsymbol{T}_{\Sigma}$ closed-loop block diagram with $\boldsymbol{F}_{eq}$

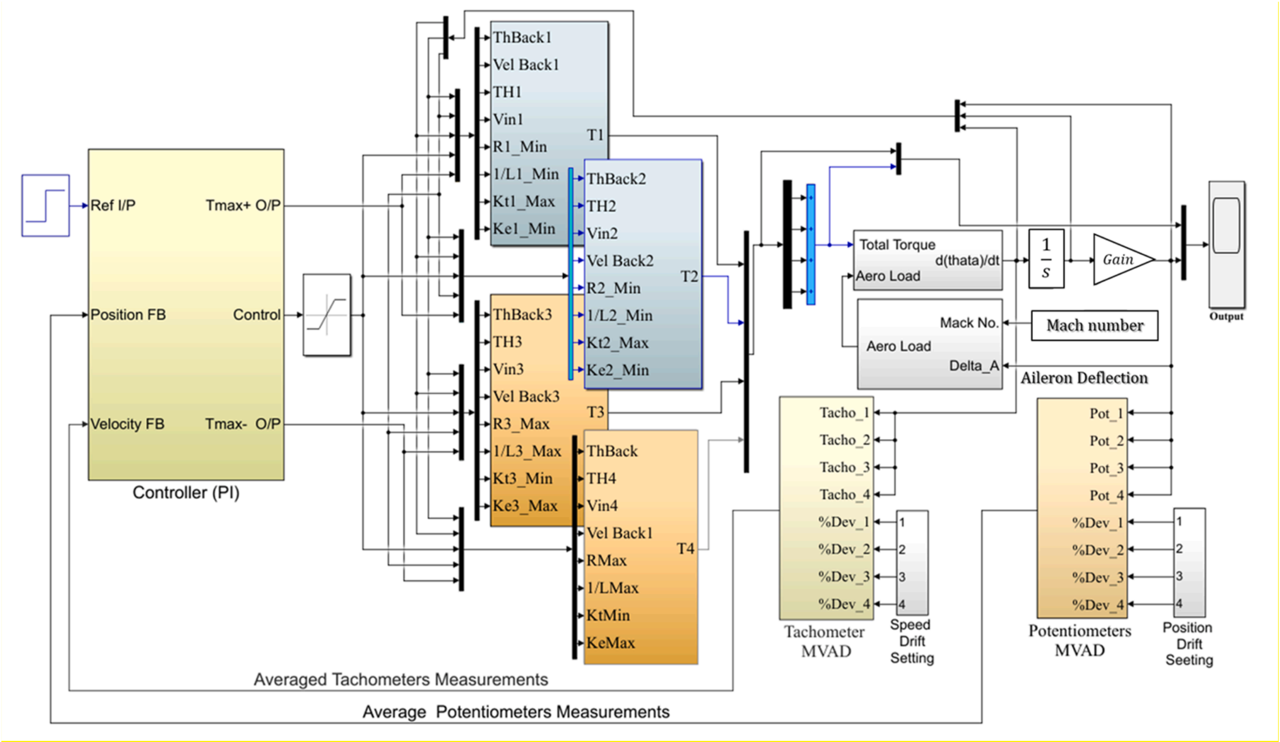

Fig. B2. T_{Σ} closed-loop block diagram with F_{eq}.

B.3 $\boldsymbol{V}_{\Sigma}$ closed-loop block diagram without $\boldsymbol{L}_{eq}$

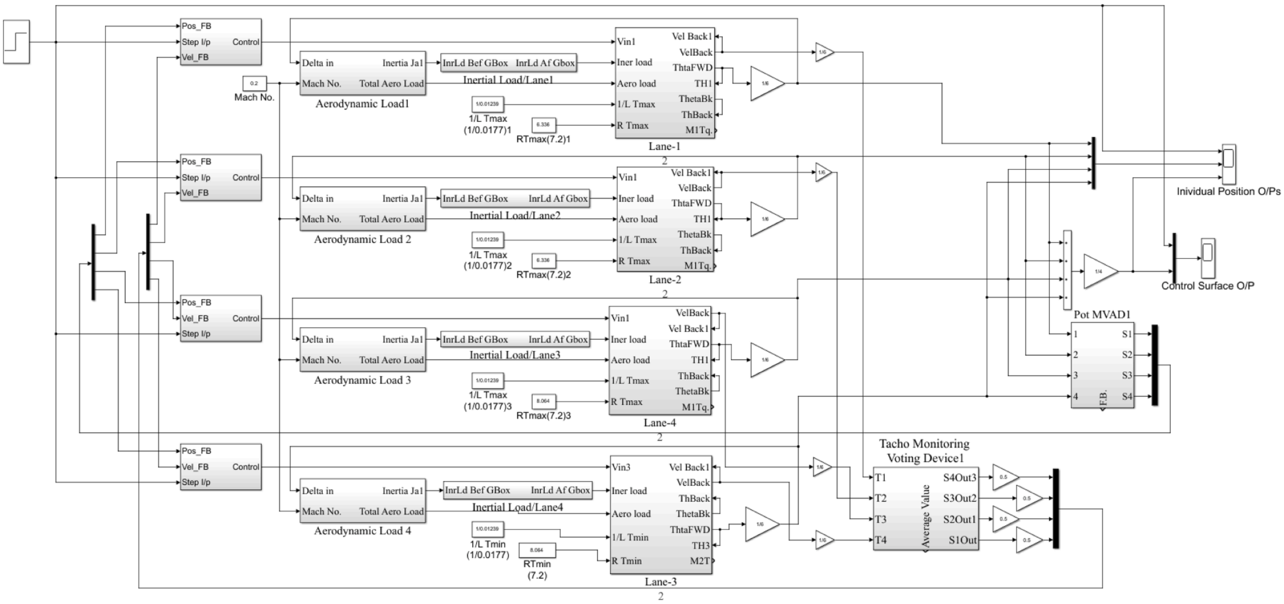

Fig. B3. V_{Σ} closed-loop block diagram without L_{eq}.

B.4 $\boldsymbol{V_\Sigma}$ *closed-loop block diagram with* $\boldsymbol{L_{eq}}$

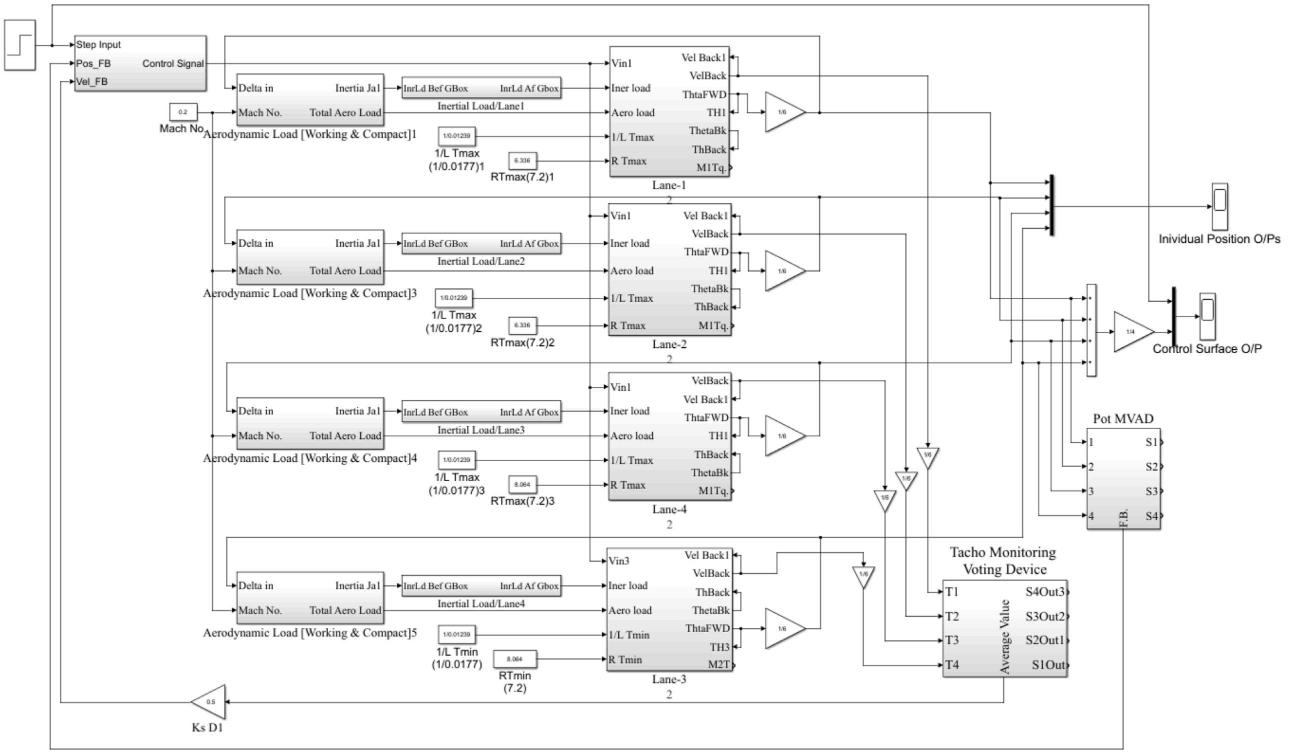

Fig. B4. V_Σ closed-loop block diagram with L_{eq}.

B. 5 *MVAD logic (potentiometers and tachometers)*

MVAD monitors lane consistency and shares commands only among healthy lanes. At each sample, residuals between lane measurements are evaluated against a predictive threshold $q_{0.9999}$ (see Section 2.4). Lanes that persistently exceed the threshold are flagged and excluded via enable masks; the averaged feedback $(\overline{\theta}, \overline{\omega})$ is then formed from the remaining healthy lanes. The sharing error $(e_T \text{ or } e_\omega)$, drives the equalisation term (F_{eq} or L_{eq}) to that adjusts lane commands. Commands are limited by saturations, masks are applied, and flags are logged for diagnostics.

Note. Current control remains per lane in the inner loop. If a motor or current-loop fault is detected by drive protection or supervisory logic, the affected lane is masked ($m_i = 0$); MVAD continues to average only θ and ω from the remaining healthy lanes.

B.6 Model summary and sources

Plant and drives. Three-phase BLDC electrical and mechanical dynamics with commutation and torque ripple, viscous/Coulomb friction, and actuator limits.

Loads. Aerodynamic and inertial loads for the inboard aileron; scenarios per Table 2.

Sensors. Position θ and speed ω with bias/drift as specified in Section 5.

Controllers. PID position control as described in Section 4.2; saturations modelled.

Where to find full equations.

- BLDC and ripple representation: [51,40,41,22,5,45,22] (motor/drive model).
- Architecture and sharing laws: Appendix A (compact forms) and Section 4.4.
- Additional background and thresholding rationale: [5] (Fig. 9; Secs. 11–13).

Data availability

No data was used for the research described in the article.

References

[1] Y. Xie, T. Antonios, Z. Dan, G. Jason, Review of hybrid electric powered aircraft, its conceptual design and energy management methodologies, Chin. J. Aeronaut. (2020).

[2] M. Boll, M. Corduan, S. Biser, M. Filipenko, Q.H. Pham, S. Schlachter, P. Rostek, M. Noe, A holistic system approach for short range passenger aircraft with cryogenic propulsion system, Supercond. Sci. Technol. 33 (4) (2020) 044014.

[3] A. Ojeda-Rodríguez, P. González-Vizuete, J. Bernal-Méndez, M.A. Martín-Prats, A survey on bidirectional DC/DC power converter topologies for the future hybrid and all electric aircrafts, Energies 13 (18) (2020) 4883.

[4] J.B. Leonard, A system look at the electromechanical actuation for primary flight control, in: NAECON, 1983.

[5] F. Annaz, Fundamental design concepts in multi-lane smart electromechanical actuators, Smart Mater. Struct. Smart Mater. Struct. 14 (2005) 1227–1238.

[6] J. Kammermann, I. Bolvashenkov, K. Tran, H.G. Herzog, I. Frenkel, Feasibility study for a full-electric aircraft considering weight, volume, and reliability

requirements, in: International Conference on Electrotechnical Complexes and Systems (ICOECS), 2020.
[7] V. Patel, C. Buccella, C. Cecati, Analysis and implementation of multilevel inverter for full electric aircraft drives, Energies 13 (22) (2020) 6126.
[8] N. Thapa, S. Ram, S. Kumar, J. Mehta, All electric aircraft: a reality on its way, Mater. Today 43 (1) (2021).
[9] H. Martin, Electric flight - potential and limitations, in: Conference: AVT-209 Workshop on Energy Efficient Technologies And Concepts Operation, 2012.
[10] K.A. Hair, Electromechanical actuation reliability and survivability, NAECON, in: NAECON, 1983.
[11] D. Ward, The all electric helicopter, in: NAECON, 1983.
[12] R. Whitaker, A. Harmon, L. Haynes, A survivable fly-by-wire spoiler actuation system featuring non-flammable fluid, 8000 psi hydraulics and direct drive valves, in: NAECON, 1985.
[13] M. Ozcan, C. Perkgoz, Deep learning-based proactive fault detection method for enhanced quadrotor safety, Aviation 28 (3) (2024) 175–187.
[14] G.S. Veresnikov, S.G. Bazhenov, I.G. Bashkirov, S.L. Chernyshev, V.I. Goncharenko, A.V. Skryabin, D.A. Petrov, Machine learning-based synthesis of diagnostic algorithms for electromechanical actuators to improve the aerospace flight safety, Acta Astronaut. 226 (2025) 239–247.
[15] D. Kim, Y. Kim, S. Kim, Numerical evaluation of structural safety of linear actuator for flap control of aircraft based on airworthiness standard, Aerospace 8 (4) (2021).
[16] Ž. Husnić, Development of aircraft mechanical systems and mechatronics modeling. *New Technologies, Development and Application III*, Bosnia and Herzegovina, Springer, Cham, 2020, pp. 147–153.
[17] S.C. Chenoweth, D.M. Fain and C.I. Svensson, “Redundant actuator development program,” Ames Research Center National Aern Autics & Space Adminstration, 1975.
[18] C.C. Chenoweth, D.R. Ryder, Redundancy of hydraulic flight control actuators. Boeing Commercial Airplane Company, NASA Technical Documents, 1976.
[19] L. Wang, J.-C. Maré, A force equalization controller for active/active redundant actuation system involving servo-hydraulic and electro-mechanical technologies, Proc. Inst. Mech. Eng. G 228 (10) (2014) 1768–1787.
[20] J. Yang, D. Hou, X. Sun, J. Zuo, Force equalization control of redundant electromechanical actuation system by FOPID and current feedforward, IEEE Access 11 (2023) 109283–109293.
[21] D. Wroble, “Force fight study in a dual electromechanical actuator configuration,” University of Dayton, Dayton, 2017.
[22] F.Y. Annaz, Force equalisation in torque-summed electromechanical actuators, Measurement 156 (2020) 16.
[23] Y. Zhao, W. Huang, F. Bu, Smart power flow node aimed at hybrid ac/dc power system for more electric aircraft, Electron. Lett. 57 (8) (2021) 334–336.
[24] O. Mesalhy, M. Elsayed, J. Corona Jr, A. Kwarteng, Study of a high-reliability dual-fan system for cooling aerospace electromechanical actuators, Therm. Sci. Eng. Prog. 18 (2020).
[25] G. Bucci, F. Ciancetta, E. Fiorucci, S. Mari, Test platform for electronic control units of high-performance safety-critical multi actuator systems, Int. J. Electr. Comput. Eng. 10 (4) (2020) 4053–4072.
[26] L. WANG, J.-C. MARE, Y. FU, Q. Haita, Force equalization for redundant active/active position control system involving dissimilar technology actuators, in: *Proceedings of the 8th JFPS International Symposium on Fluid Power*, Okinawa, 2011.
[27] L. Qu, N. Li, J.H. Ye, Y.P. Xu, Equalization control of rudder force fight under hydraulic servo-actuation system, J. Phys. 2569 (012069) (2023).
[28] W.U. Rehman, X. Wang, Y. Cheng, H. Chai, Z. Hameed, X. Wang, F. Saleem, E. Lodhi, Motion synchronization for the SHA/EMA Hybrid actuation system by using an optimization algorithm, Automatika 62 (3–4) (2021) 503–512.
[29] L. Wang, “Force equalization for active/active redundant actuation system involving servo-hydraulic and electromechanical technologies,” Université de Toulouse; Institut National des Sciences Appliq, Toulouse, December 2012.
[30] J.R. Hoffman, “Passive load testing for evaluation of electromechanical actuators,” Air Force Institute of Technology, March 2018.
[31] W.E. Boehringer, T. Verhoeven and W. William, “Mechanically redundant actuator assembly”. US Patent 5701,801, 30 Dec 1997.
[32] Y. Lin, E. Baumann, D. Bose, R. Beck and G. Jenney, “Tests and techniques for characterizing and modeling X-43A electromechanical actuators,” NASA Dryden Flight Research Center;, Edwards, CA, United States, 01 Dec 2008.
[33] C. Wang, L. Tao, Y. Ding, C. Lu, J. Ma, An adversarial model for electromechanical actuator fault diagnosis under nonideal data conditions, Neural Comput. Appl. 34 (2022) 5883–5904.
[34] D.Y. Wang, D.Q. Li, J. Chen, S.C. Zheng, A position synchronization control for dual redundant electro-mechanical actuation in flight control system, in: IOP Conf. Series: Materials Science and Engineering, 2019.
[35] X. Hu, T. Tang, L. Tan, H. Zhang, Fault detection for point machines: a review, challenges, and perspectives, Actuators 12 (391) (2023).
[36] W. Rehman, X. Wang, S. Wang, I. Azhar, Motion synchronization of HA/EHA system for a large civil aircraft by using adaptive control, in: *IEEE Chinese Guidance, Navigation and Control Conference*, Nanjing,China, 2016.
[37] V.D.D. Bossche, The A380 flight control electrohydrostatic actuators, achievements and lessons learnt, in: Proc. 25th Congress of the International Council of the Aeronautical Sciences, 2006.
[38] G. Di Rito, F. Schettini, Health monitoring of electromechanical flight actuators via position-tracking predictive models, Adv. Mech. Eng. 10 (4) (2018) 1–12.
[39] G. Di Rito, R. Galatolo, F. Schettini, Self-monitoring electro-mechanical actuator for medium altitude long endurance unmanned aerial vehicle flight controls, Adv. Mech. Eng. 8 (5) (2016) 1–11.
[40] F.Y. Annaz, M.M. Kaluarachchi, Progress in redundant electromechanical actuators for aerospace applications, Aerospace 10 (787) (2023).
[41] F.Y. Annaz, The impact of force equalization in minimizing the effect of drift in feedback transducers in torque-summed electromechanical actuators, Eng. Sci. Technol. Int. J. Vols, 492024101597 (101597) (2024).
[42] RTCA, Environmental Conditions and Test Procedures For Airborne Equipment, Section 4, RTCA, Inc. (Radio Technical Commission for Aeronautics), Washington, DC, 2010.
[43] Mil-F-83300, flying qualities of piloted VSTOL aircraft, 1970.
[44] Mil-C-18244, flying qualities of piloted VSTOL aircraft, 1970.
[45] F. Annaz, Worthy test programs and developments in smart electromechanical actuators, Smart Mater. Struct. 16 (2007).
[46] I.M.D. Publication, “Kollmorgen SILVERLINETM Brushless Series Motors,” Kollmorgen Motion Technologies Group, 1989. [Online]. Available: https://www.kollmorgen.com/sites/default/files/public_downloads/Silverline%20Motor%20Catalog.pdf. [Accessed 19 Dec 2024].
[47] kollmorgen, “Kollmorgen: aerospace and defense,” [Online]. Available: https://www.kollmorgen.com/en-us/solutions/aerospace-and-defense/aerospace-defense/. [Accessed 19 Dec 2024].
[48] M. Inc., “Rotary variable differential transformer (RVDT),” 2019. [Online]. Available: https://www.moog.com/literature/MCG/RVDTDtS.pdf. [Accessed 19 Dec 2024].
[49] M. Inc., “Rotary variable differential transformer,” 2019. [Online]. Available: https://www.moog.com/products/rotary-variable-differential-transformers-rvdts-0. [Accessed 19 Dec 2024].
[50] M.I. Research, “Rotary variable differential transducer,” 2019. [Online]. Available: https://www.mtcind.com/mtc-rvdt-116. [Accessed 19 Dec 2024].
[51] F.Y. Annaz, Design and Development of Multi-Lane Smart Electromechanical Actuators, The Institution of Engineering and Technology, London, 2014.